applied sciences

MDPI

Article

Erosion Behavior and Structural Optimization of a Drill-Bit-Integrated Vibration Detection Tool Based on CFD–DPM

Jizhou Jia [1,2], Lei Shi [1,2,*], Chen Yu [3], Zhihao Jiang [1,2] and Yinlong Xie [1,2]

[1] School of Mechanical Engineering, Yangtze University, Jingzhou 434023, China; 2025710687@yangtzeu.edu.cn (J.J.); 2025710705@yangtzeu.edu.cn (Y.X.)
[2] Hubei Engineering Research Center for Oil & Gas Drilling and Completion Tools, Jingzhou 434023, China
[3] Engineering Technology Research Institute, CNPC Bohai Drilling Engineering Co., Ltd., Tianjin 300280, China
* Correspondence: shilei0909@163.com

Abstract

Drill-bit-integrated vibration sensors face localized erosion from sand-laden drilling fluid. We applied a computational fluid dynamics–discrete phase model (CFD–DPM) incorporating the realizable k–ε turbulence, Forder rebound, and Oka erosion models to analyze erosion and optimize tool geometry. Erosion was concentrated at channel transitions and guide-bracket roots. Among the investigated conditions, inlet velocity produced the largest variation in predicted erosion, and 200 μm particles generated the highest erosion among four tested sizes. An optimized design with a 45° semi-conical guide hood, two guide brackets, and a 4 mm root fillet reduced the predicted maximum erosion flux from 7.62×10^{-4} to 2.21×10^{-4} kg·m^{-2}·s^{-1}, or approximately 71%. Sampling variability was assessed through five DPM repeats per condition; fine-grid convergence indices were 1.88% and 2.94% for the baseline and optimized geometries, respectively. Prototype tests confirmed signal acquisition and rotation tracking. Sand-laden erosion tests at 15 m·s^{-1}, 100 μm, and 0.01 kg·s^{-1}, using three specimens per geometry and 1800 s exposure, showed 56.72% lower overall mass-loss rate and 69.54% lower registered local-window depth rate. These short-duration measurements support erosion mitigation, but do not directly validate the predicted peak-flux reduction.

Keywords: drill-bit-integrated vibration detection tool; erosion wear; CFD–DPM; Oka model; structural optimization

Check for updates

Academic Editor: Dan Sui

Received: 12 October 2026
Revised: 28 October 2026
Accepted: 2 November 2026
Published: 5 November 2026

Copyright: © 2026 by the authors. Licensee MDPI, Basel, Switzerland. This article is an open access article distributed under the terms and conditions of the Creative Commons Attribution (CC BY) license.

1. Introduction

During the drilling of deep, ultra-deep, and complex-trajectory wells, strong nonlinear interactions occur between the drill bit and the formation. These interactions readily induce harmful vibrations, such as axial bit bounce, lateral whirl, and torsional stick-slip. Drill-string vibration not only reduces the rate of penetration and wellbore quality, but may also lead to cutter damage, fatigue failure of the bottom-hole assembly, and abnormal failure of downhole measurement tools [1–4]. Therefore, accurate acquisition of near-bit vibration information is an important basis for drilling-state identification, drilling-parameter optimization, and drilling-tool failure warning.

Previous work on drill-string vibration acquisition, downhole dynamic measurement, and memory-type vibration measurement tools has shown that downhole vibration measurement is important for judging the working state of drilling tools, identifying abnormal vibration, and optimizing drilling parameters [5]. Conventional measurement-while-drilling

tools are usually installed as subs at a certain distance from the bit. Because bit vibration signals attenuate and lag during transmission through the drill-string structure owing to bending and damping, the measurement accuracy may be insufficient [6–8]. By contrast, installing a vibration detection tool directly in the central waterway or shank region of the drill bit places the sensor closer to the bottom-hole vibration source, which may reduce transmission-related attenuation and delay.

However, the integrated arrangement places the tool's external surfaces in particle-laden drilling-fluid flow, creating a risk of solid-particle erosion. This wear mechanism arises from repeated particle–wall impacts and is a recognized concern in oil- and gas-handling equipment [9]. Changes in flow-path geometry can affect particle transport and local impact conditions, thereby modifying the erosion distribution [9].

In the present design, drilling fluid is diverted by the guide hood into the annular passage between the tool body and external mounting sleeve, bypasses the guide brackets, and then flows toward the bit crown and nozzles (Figure 1). These features introduce changes in passage area and flow direction that may alter particle trajectories and wall-impact conditions. Their influence on localized erosion therefore requires analysis for the actual tool geometry, consistent with geometry-dependent particle-impact behavior reported for control valves and combined CFD/experimental studies [10,11].

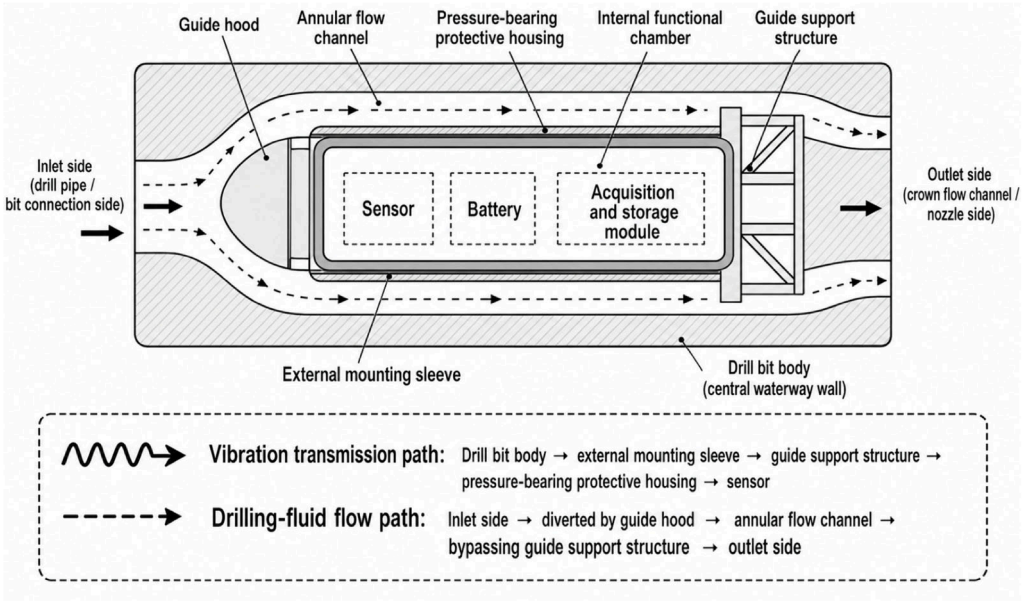


Figure 1. Schematic diagram of the tool installation position and drilling-fluid flow path.

Solid-particle erosion theory indicates that erosion of ductile metals is closely related to particle impact velocity, impact angle, particle size, target hardness, and particle impact frequency [12–18]. Reviews and numerical studies have shown that the computational fluid dynamics–discrete phase model (CFD–DPM), combined with empirical or semi-empirical erosion models, can effectively analyze particle trajectories, wall impact positions, and local erosion distributions [9,10]. The realizable k-ε turbulence model is suitable for engineering analysis of complex internal turbulent flows involving streamline curvature and local separation [19]. Mechanistic erosion equations, combined CFD-experimental methodologies, and bend erosion experiments have further promoted erosion prediction in complex flow passages [11,20,21]. At the same time, structural modification has been widely regarded as an effective approach for reducing local erosion peaks. Geometry-specific mitigation has been investigated using a vortex chamber [22], while correlations for bends and multiphase equipment illustrate the dependence of erosion assessment on

flow configuration [23,24]. In addition, studies on subsea choke valves, gas-storage tubing strings, and erosion-resistant coatings have indicated that structural optimization and surface protection are important strategies for improving the service life of equipment exposed to sand-laden flow environments [25–27].

Numerical work on a vortex-chamber elbow demonstrates that a change in passage geometry can modify particle transport and mitigate erosion in gas–solid flow [22]. Complementary liquid–solid experiments at 2.5 $m \cdot s^{-1}$ linked particle-trajectory deviations to differences in local erosion morphology [28]. These studies provide a mechanistic rationale for geometry-specific assessment, while their erosion patterns cannot be transferred directly to high-velocity drilling-fluid flow. For the present tool, the guide hood, annular passage divided by guide brackets, bracket-root fillets, and local passage transitions raise the question of how geometry controls particle–wall impacts and localized erosion, and which modifications improve erosion resistance while maintaining hydraulic performance.

This study identifies erosion-prone regions in a drill-bit-integrated vibration detection tool, analyzes parameter responses, and compares structural alternatives to balance predicted erosion resistance and hydraulic performance. Sand-laden tests compare overall mass loss and registered local wear depth for the baseline and optimized flow passages, while prototype tests assess the optimized tool's sensing function.

2. Materials and Methods

2.1. Tool Installation, Working Principle, and Computational Model

The drill-bit-integrated vibration detection tool is coaxially installed along the central axis inside the central waterway of a 241 mm polycrystalline diamond compact (PDC) drill bit. The tool is positioned axially between the bit connection thread root and the flow-dividing region of the bit crown. This location is close to the bottom-hole rock-breaking vibration source and does not directly occupy the cutter-blade space; the arrangement is intended to acquire near-bit vibration signals while preserving the cutter-blade space. The tool installation position and drilling-fluid flow path are shown in Figure 1.

During operation, the internal functional chamber is sealed inside the pressure-bearing housing and mainly accommodates a single-axis IEPE piezoelectric accelerometer (353B01, PCB Piezotronics, Inc., Depew, NY, USA), a battery, and a signal-acquisition and storage module. Axial, lateral, and torsional vibration generated during bit-rock interaction is transmitted through the bit body to the external mounting sleeve, then through the guide brackets and pressure-bearing housing to the sensor. The installed accelerometer records the vibration component along its sensitive axis. The sensor converts mechanical vibration into electrical signals, which are recorded by the internal acquisition and storage module. In other words, vibration measurement occurs inside the sealed functional chamber, and drilling fluid does not enter the chamber.

The drilling-fluid flow path is as follows. Sand-laden drilling fluid first enters the bit central waterway from the drill pipe and bit connection side. It is divided by the guide hood at the head of the tool and then enters the annular flow passage between the tool body and the external mounting sleeve. The fluid bypasses the guide brackets and their root-transition regions, continues downstream, and finally enters the bit crown flow passage before being discharged through the nozzles toward the bottom hole. The guide hood weakens direct impact on the upstream end of the tool, the annular channel maintains drilling-fluid circulation, and the guide brackets simultaneously provide positioning, support, and vibration transmission.

The baseline structure uses a hemispherical guide hood, three guide brackets, and a 3 mm bracket-root fillet. The main structural parameters of the baseline model are listed in Table 1. The baseline and optimized specimens were custom-machined to the design

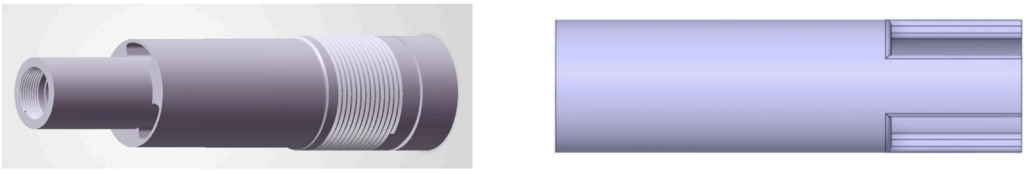
drawings from 42CrMo alloy structural steel (Baoshan Iron & Steel Co., Ltd., Shanghai, China) and heat-treated to a nominal Vickers hardness of 320 HV.

Table 1. Main structural parameters of the drill-bit-integrated vibration detection tool.

Parameter	Value
Outer diameter of pressure housing	48 mm
Wall thickness of pressure housing	6.5 mm
Total tool length	324 mm
Outer diameter of external mounting sleeve	76.2 mm
Wall thickness of external mounting sleeve	3.5 mm
Guide bracket thickness	9.6 mm
Baseline fillet radius	3 mm
Minimum annular channel width	10.6 mm

The structure provides a drilling-fluid passage and installation space for the internal sensors and electronic components. The computational domain represented the drilling-fluid passage around the pressure housing, including the annular passage between the housing and external mounting sleeve; the sealed functional chamber was excluded. In the physical assembly, the sleeve is threaded to the drill bit, and a threaded end cap with a sealing ring closes the chamber. Individual thread profiles inside the drill bit, small chamfers, and minor assembly details were not explicitly resolved to reduce geometric and meshing complexity. The principal flow-passage boundaries, guide hood, guide brackets, and channel transitions were retained. Flow-passage transition fillets, including those at the bracket roots, were explicitly represented and were distinct from the omitted small chamfers. The three-dimensional geometry was created using SOLIDWORKS 2022 (Dassault Systèmes SOLIDWORKS Corp., Waltham, MA, USA).

The simplifications support comparison of the retained flow-passage features, but omitted wetted details may alter near-wall flow, particle trajectories and peak erosion. Their influence was not quantified; the mesh study in Section 2.2 addresses discretization rather than omitted geometry. Excluding a sealed, non-wetted chamber differs from approximating a wetted surface, and small feature size alone does not establish a negligible erosion effect. The predictions do not resolve wear at omitted threads or assembly details. Figure 2 shows the structure and computational domain.



(**a**) (**b**)

Figure 2. Structure and computational domain of the drill-bit-integrated vibration detection tool: (**a**) tool structure; (**b**) computational-domain detail.

2.2. Mesh Generation and Mesh-Sensitivity Assessment

We prepared the computational meshes using ANSYS Meshing 2022 R1 (Ansys, Inc., Canonsburg, PA, USA) and performed the flow-field, particle-tracking and erosion calculations using ANSYS Fluent 2022 R1 (Ansys, Inc., Canonsburg, PA, USA). The computational domain was discretized with polyhedral unstructured meshes. We locally refined the channel transition, bracket roots and tool wall, where large velocity gradients and concentrated particle impacts are expected. The root-transition regions include the fillet surfaces represented in the geometric model. Boundary-layer meshes were generated near the wall

to improve the accuracy of wall shear and near-wall particle-motion calculations. Ten boundary-layer cells were used, with a first-layer height of 0.02 mm and a growth rate of 1.1. The computational mesh and local refinement are shown in Figure 3.

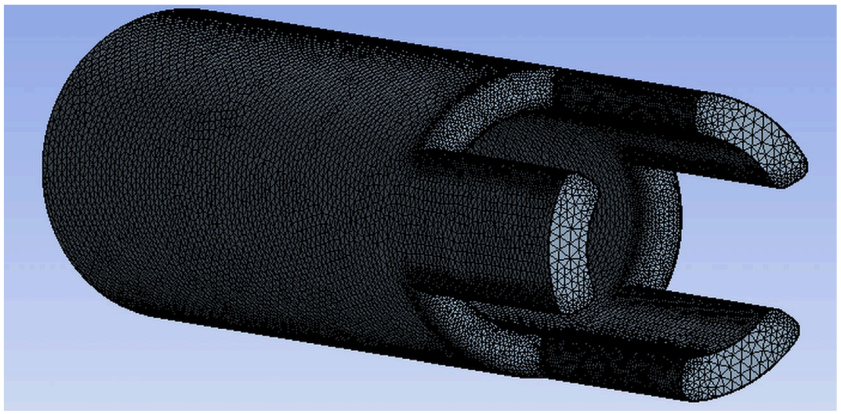


Figure 3. Computational grid and local refinement.

We evaluated pressure drop and area-averaged erosion on five mesh-density schemes to select the production mesh. Table 2 reports these mesh-sensitivity results.

Table 2. Mesh-sensitivity assessment results.

Scheme	Mesh Number	Inlet Pressure Drop (MPa)	Pressure-Drop Change (%)	Average Erosion Rate (10^{-7} kg·m^{-2}·s^{-1})	Mean-Erosion Change (%)
1	333,457	3.03	-	5.47	-
2	524,197	3.10	2.31	6.81	24.50
3	648,629	3.15	1.61	7.20	5.73
4	839,941	3.22	2.22	8.10	12.50
5	1,170,848	3.26	1.24	7.86	2.96

Table 2 shows increasing pressure drop and a non-monotonic area-averaged erosion response as the mesh number increases. Between 839,941 and 1,170,848 cells, the pressure-drop variation is 1.24% and the average-erosion variation is 2.96%, both below 5%. We selected the 839,941-cell mesh for the production calculations as a compromise between computational cost and these observed changes. These pressure-drop and area-averaged erosion comparisons do not establish grid convergence of the local maximum erosion flux or a total numerical uncertainty bound. In Table 2, each relative change is the absolute difference from the preceding mesh result divided by that preceding value; these changes are not errors against a known exact solution.

We used the local maximum erosion rate, E_{max}, as the primary optimization index. To assess its sensitivity to mesh resolution, we performed a separate three-dimensional grid-convergence-index (GCI) analysis for the baseline and final optimized geometries [29]. We describe the method below and report the results in Section 3.4.5.

For each geometry, the systematic refinement sequence comprised 526,744, 1,157,257 and 2,542,889 polyhedral cells (coarse, medium and fine). The fluid-domain volumes were 8.314×10^{-4} m^3 for the baseline and 8.462×10^{-4} m^3 for the optimized geometry. Global sizes were 2.860, 2.200 and 1.6923 mm; bracket-root sizes were 0.338, 0.260 and 0.200 mm; first-layer heights were 0.02600, 0.02000 and 0.01538 mm, respectively. Ten wall layers and a growth rate of 1.1 were retained. Within each geometry, we retained the flow-passage boundaries and fillet radii while refining the mesh, so the baseline and final optimized geometries formed separate refinement sequences. The global and bracket-root

sizes describe overall and local mesh controls, respectively, while the first-layer heights specify wall-normal resolution. These mesh controls are distinct from the volume-based effective spacing h used in the GCI calculation. Enhanced wall treatment was used. The median y^+ values were 9.2, 7.1 and 5.5, with 95th percentiles of 62.4, 48.6 and 37.8.

We defined the monitored quantity φ as the arithmetic mean of the maximum wall-face erosion flux from five calculations on each mesh. For each calculation, we first extracted the maximum over the same physical wall set, including the bracket-root and fillet surfaces, and then averaged the five maxima. Each calculation tracked 2,000,000 particle-parcel trajectories. Residuals were $\leq 10^{-5}$, mass imbalance was $\leq 0.05\%$, and the final 500-step peak drift was $\leq 0.05\%$. Fine, medium and coarse meshes are indexed 1, 2 and 3. The effective three-dimensional spacing $h = (V/N)^{1/3}$ uses the fluid-domain volume V and total cell count N; $h_1 < h_2 < h_3$. The refinement ratios are defined as follows.

$$h = \left(\frac{V}{N}\right)^{1/3};\ r_{21} = \frac{h_2}{h_1};\ r_{32} = \frac{h_3}{h_2} \tag{1}$$

For each monotonic sequence, the observed order p was solved from Equation (2) using unrounded h values and a leading discretization-error term proportional to h^p. Here $\varepsilon_{21} = \varphi_2 - \varphi_1$ and $\varepsilon_{32} = \varphi_3 - \varphi_2$. The order p is estimated from the three results rather than fixed at the formal order of the discretization scheme.

$$\frac{\varepsilon_{32}}{\varepsilon_{21}} = \frac{h_3^p - h_2^p}{h_2^p - h_1^p};\ \varepsilon_{21} = \varphi_2 - \varphi_1 \tag{2}$$

Richardson extrapolation and the fine-grid GCI were evaluated using Equations (3) and (4), with safety factor $F_s = 1.25$ for three grids [29]. The medium-grid index GCI_{32} was calculated analogously using r_{32} and φ_2 as the refinement ratio and relative-error denominator, respectively, for the asymptotic-ratio check in Section 3.4.5.

$$\varphi_{ext} = \frac{r_{21}^p \varphi_1 - \varphi_2}{r_{21}^p - 1} \tag{3}$$

$$GCI_{21} = \frac{F_s \left|\frac{\varphi_2 - \varphi_1}{\varphi_1}\right|}{r_{21}^p - 1} \times 100\% \tag{4}$$

We evaluated peak-flux convergence for the baseline and final optimized geometries using these independent refinement sequences. The 839,941-cell production mesh is not a member of the sequences. We therefore interpret their fine-grid GCIs as discretization-uncertainty estimates for the corresponding fine-grid peak means, rather than error bars for the production-grid E_{max} values. These estimates exclude particle-sampling variation, physical-input uncertainty and erosion-model error, and do not establish grid convergence for every intermediate geometry or operating condition.

2.3. Governing Equations and Turbulence Model

The Euler–Lagrange method was used to describe the solid–liquid two-phase flow of drilling fluid and particles. The drilling fluid was treated as the continuous phase and solved in the Eulerian coordinate system, whereas solid particles were treated as the discrete phase and tracked in the Lagrangian coordinate system. The drilling fluid was considered an incompressible Newtonian fluid. The mass-conservation equation is

$$\frac{\partial \rho}{\partial t} + \frac{\partial (\rho u)}{\partial x} + \frac{\partial (\rho v)}{\partial y} + \frac{\partial (\rho w)}{\partial z} = 0 \tag{5}$$

where ρ is the fluid density ($kg \cdot m^{-3}$); t is time (s); x, y, and z are the three spatial coordinate directions; and u, v, and w are the corresponding velocity components. The momentum-conservation equation can be written as

$$\begin{cases} \frac{\partial(\rho u_x)}{\partial t} + \nabla \cdot \left(\rho u_x \vec{v}\right) = -\frac{\partial P}{\partial x} + \frac{\partial \tau_{xx}}{\partial x} + \frac{\partial \tau_{yx}}{\partial y} + \frac{\partial \tau_{zx}}{\partial z} + F_x, \\ \frac{\partial(\rho u_y)}{\partial t} + \nabla \cdot \left(\rho u_y \vec{v}\right) = -\frac{\partial P}{\partial y} + \frac{\partial \tau_{xy}}{\partial x} + \frac{\partial \tau_{yy}}{\partial y} + \frac{\partial \tau_{zy}}{\partial z} + F_y, \\ \frac{\partial(\rho u_z)}{\partial t} + \nabla \cdot \left(\rho u_z \vec{v}\right) = -\frac{\partial P}{\partial z} + \frac{\partial \tau_{xz}}{\partial x} + \frac{\partial \tau_{yz}}{\partial y} + \frac{\partial \tau_{zz}}{\partial z} + F_z. \end{cases} \quad (6)$$

where P is pressure, τ_{ij} denotes a viscous-stress component, and F_i is the body force per unit volume ($N \cdot m^{-3}$) in direction i. In Equation (6), v denotes the fluid-velocity vector, with components u_x, u_y, and u_z; these correspond to u, v, and w in Equation (5). The general total-energy balance is

$$\frac{\partial(\rho E)}{\partial t} + \nabla \cdot \left(\vec{v}(\rho E + P)\right) = \nabla \cdot \left(k_{eff} \nabla T - \sum_j h_j \vec{J}_j + \left(\tau_{eff} \cdot \vec{v}\right) \right) + S_h \quad (7)$$

where E in Equation (7) is the total energy per unit mass, P is pressure, v is the fluid-velocity vector, T is temperature, k_{eff} is the effective thermal conductivity, and τ_{eff} is the effective stress tensor. The symbols h_j and $\boldsymbol{J}_j$ denote the specific enthalpy and diffusion-flux vector of species j, respectively. S_h is the volumetric energy-source term, and the stress-work flux is $\tau_{eff} \cdot v$, whose divergence appears in Equation (7).

The internal flow path of the tool contains local turning, contraction, bracket obstruction, recirculation, and enhanced shear. The realizable k-ε turbulence model was therefore used for the continuous phase. This model introduces realizability constraints and improves the prediction of shear flows, rotating flows, and separated flows, making it suitable for the complex internal turbulent flow investigated in this study. For the realizable k-ε model, the transport equations for turbulent kinetic energy k and dissipation rate ε are

$$\begin{cases} \frac{\partial(\rho k)}{\partial t} + \frac{\partial(\rho k u_i)}{\partial x_i} = \frac{\partial}{\partial x_j}\left[\left(\mu + \frac{\mu_t}{\sigma_k}\right)\frac{\partial k}{\partial x_j}\right] + G_k + G_b + S_k - Y_M - \rho\varepsilon \\ \frac{\partial(\rho \varepsilon)}{\partial t} + \frac{\partial(\rho \varepsilon u_i)}{\partial x_i} = \frac{\partial}{\partial x_j}\left[\left(\mu + \frac{\mu_t}{\sigma_\varepsilon}\right)\frac{\partial \varepsilon}{\partial x_j}\right] + C_{1\varepsilon}\frac{\varepsilon}{k}C_{3\varepsilon}G_b - C_2\rho\frac{\varepsilon^2}{k+\sqrt{\nu\varepsilon}} + \rho C_1 S\varepsilon + S_\varepsilon \end{cases} \quad (8)$$

where k is turbulent kinetic energy per unit mass ($m^2 \cdot s^{-2}$), ε is its dissipation rate ($m^2 \cdot s^{-3}$), and u_i is the mean-velocity component in direction x_i. The symbols μ and μ_t denote molecular and turbulent dynamic viscosity. G_k and G_b are turbulent-energy production by mean shear and buoyancy, respectively, and Y_M is the dilatational contribution. $S = (2S_{ij}S_{ij})^{1/2}$ is the mean strain-rate magnitude, with $S_{ij} = (\partial u_i/\partial x_j + \partial u_j/\partial x_i)/2$, and $\nu = \mu/\rho$ is kinematic viscosity. The symbols σ_k and σ_ε are turbulent Prandtl numbers. C_1 is a strain-dependent turbulence-model coefficient; C_2, $C_{1\varepsilon}$, and $C_{3\varepsilon}$ are the other turbulence-model coefficients, and S_k and S_ε are source terms. The incompressible constant-density specialization has no dilatational contribution [19].

2.4. Discrete Phase Model and Particle–Wall Collision

We represented sand particles as spheres in the discrete phase model (DPM). In the Lagrangian coordinate system, the particle-motion equation is

$$\frac{d\vec{v}_p}{dt} = F_D\left(\vec{v} - \vec{v}_p\right) + \frac{\vec{g}\left(\rho_p - \rho\right)}{\rho_p} + \vec{F}_{vm} + \vec{F}_{pg} + \vec{F}_{lift} \quad (9)$$

where v is the mean fluid-velocity vector, v_p is the particle-velocity vector, and ρ and ρ_p are fluid and particle densities. F_D is a drag coefficient with units of s^{-1}, so $F_D(v - v_p)$ is drag acceleration; g denotes gravitational acceleration. $\boldsymbol{F}_{vm}$, $\boldsymbol{F}_{pg}$, and $\boldsymbol{F}_{lift}$ in Equation (9) are the

virtual-mass, pressure-gradient, and lift contributions per unit particle mass, respectively. The drag coefficient is expressed as

$$F_{\mathrm{D}} = \frac{18\mu}{\rho_{\mathrm{p}} d_{\mathrm{p}}^2} \frac{\mathrm{C_D} Re_{\mathrm{p}}}{24} \tag{10}$$

$$Re_{\mathrm{p}} = \frac{\rho d_{\mathrm{p}}}{\mu} \left\| \vec{v} - \vec{v}_{\mathrm{p}} \right\| \tag{11}$$

$$C_{\mathrm{D}} = \mathrm{a}_1 + \frac{\mathrm{a}_2}{\mathrm{Re}_{\mathrm{p}}} + \frac{\mathrm{a}_3}{\mathrm{Re}_{\mathrm{p}}^2} \tag{12}$$

where d_{p} is particle diameter, Re_{p} is the relative particle Reynolds number, μ is fluid dynamic viscosity, and C_{D} is the dimensionless spherical-particle drag coefficient. Equation (12) has the piecewise form of the Morsi–Alexander correlation [30]; a_1, a_2, and a_3 are the piecewise empirical coefficients for the applicable Re_{p} interval. They are distinct from the turbulence coefficients in Equation (8) and the regression coefficients in Equation (21). The applicable coefficient interval must be selected using the local particle Reynolds number, rather than assigning a single set to every trajectory.

We used the Forder correlations [10] to approximate energy loss in inelastic particle–wall collisions without resolving individual grain contact geometry or orientation. The normal and tangential restitution coefficients are

$$e_{\mathrm{n}} = \frac{\left| v_{p2,n} \right|}{\left| v_{p1,n} \right|} = 0.988 - 0.78\alpha + 0.19\alpha^2 - 0.024\alpha^3 + 0.027\alpha^4 \tag{13}$$

$$e_{\mathrm{t}} = \frac{v_{p2,t}}{v_{p1,t}} = 1.0 - 0.78\alpha + 0.84\alpha^2 - 0.21\alpha^3 + 0.028\alpha^4 - 0.022\alpha^5 \tag{14}$$

where e_{n} and e_{t} are the normal and tangential restitution coefficients, respectively; α is measured from the wall tangent in radians, and v_{p1} and v_{p2} denote particle velocities immediately before and after impact. The normal coefficient uses the magnitudes of the normal components because the normal direction reverses. These correlations were developed for AISI 4130 steel [10]; their application to 42CrMo is a modeling approximation.

We assessed DPM repeat-to-repeat variation using five tracking calculations for each of 12 distinct operating conditions. For each condition, we held the converged carrier-phase field fixed and used discrete random-walk tracking with the Forder rebound treatment. Each repeat used 200,000 trajectories, a step-length factor of 5 and a maximum of 50,000 tracking steps. The five calculations are identified as 17, 43, 79, 113 and 167 in Table 3. The residual threshold was 10^{-5}, inlet–outlet mass imbalance was ≤0.05%, and the final 500-step pressure-drop drift was ≤0.10%. We extracted E_{max} as the maximum face value over the same full wall set.

For condition i, each plotted center $E_{0,\mathrm{i}}$ is the corresponding production-grid calculation, rather than the repeat mean. The lower and upper limits are the extrema across that value and the five DPM repeat values:

$$E_{\mathrm{low},i} = \min\{E_{0,i}, E_{i,1}, \ldots, E_{i,n}\} \tag{15}$$

$$E_{\mathrm{high},i} = \max\{E_{0,i}, E_{i,1}, \ldots, E_{i,n}\} \tag{16}$$

Here $n = 5$, and the asymmetric bar lengths are $E_{0,\mathrm{i}} - E_{\mathrm{low,i}}$ and $E_{\mathrm{high,i}} - E_{0,\mathrm{i}}$. These observed minimum–maximum ranges summarize the recorded DPM spread at fixed carrier-phase conditions and have no specified coverage probability. They are neither SD nor confidence or total-uncertainty intervals and exclude grid-discretization and physical-model errors. The shared baseline B0 (15 m·s^{-1}, 100 µm, 0.01 kg·s^{-1}) uses the same five records in

all three parameter-response plots, so the 14 plotted points represent 12 distinct conditions and 60 DPM repeats. Tables 3 and 4 list the repeat results and range limits.

Table 3. Five DPM repeat results per distinct condition.

ID	17	43	79	113	167
U5	0.5616	0.5749	0.5838	0.5859	0.6042
U10	2.8455	2.8691	2.8648	2.8539	2.8251
B0	7.3663	7.6534	7.5278	8.1987	7.7536
U20	20.3786	18.9199	19.5189	19.2767	20.0210
U25	27.8419	28.9216	30.4313	29.2145	30.0460
D200	17.5512	18.1081	18.7517	18.0339	18.0418
D300	13.6368	13.7825	13.3985	14.1123	12.9148
D400	13.3509	13.2035	13.5629	13.8758	13.7016
Q005	3.6166	3.7078	3.5855	3.4958	3.5051
Q015	11.0692	10.2510	11.1105	10.6733	10.8607
Q020	14.4445	14.7989	14.1956	14.0983	14.9780
Q025	18.4079	17.8084	17.7320	18.9384	18.2929

Table 4. Production-grid centers and observed minimum–maximum limits used in the parameter-response plots.

ID	$E_{0,i}$	$E_{low,i}$	$E_{high,i}$
U5	0.57	0.5616	0.6042
U10	2.81	2.8100	2.8691
B0	7.62	7.3663	8.1987
U20	19.60	18.9199	20.3786
U25	29.20	27.8419	30.4313
D200	18.50	17.5512	18.7517
D300	13.60	12.9148	14.1123
D400	13.30	13.2035	13.8758
Q005	3.56	3.4958	3.7078
Q015	10.70	10.2510	11.1105
Q020	14.30	14.0983	14.9780
Q025	17.80	17.7320	18.9384

Flux values in Tables 3 and 4 are in 10^{-4} kg·m^{-2}·s^{-1}. All cases use the baseline geometry. U, D and Q identify changes in inlet velocity (m·s^{-1}), particle diameter (μm) and sand mass flow rate (kg·s^{-1}), respectively; the other inputs remain at their shared baseline values. Record identifiers label repeat calculations, not independent operating conditions.

2.5. Erosion Model

The Oka erosion model [17,18] was used to predict wall erosion rate. This model accounts for particle impact velocity, impact angle, particle size, and target material hardness, and is suitable for erosion prediction of ductile metals under solid-particle impact. The underlying per-impact erosion ratio is expressed as

$$E = E_{90} \cdot g(\alpha) \tag{17}$$

$$E_{90} = K \cdot (h_v)^{k_1} \cdot \left(\frac{v}{v_0}\right)^{k_2} \cdot \left(\frac{d_p}{d_0}\right)^{k_3} \tag{18}$$

$$g(\alpha) = (\sin\alpha)^{n_1} \cdot [1 + h_v \cdot (1 - \sin\alpha)]^{n_2} \tag{19}$$

where E in Equations (17)–(19) is the eroded wall volume per unit incident particle mass (mm^3·kg^{-1}), and E_{90} is that ratio at normal incidence for the current particle impact speed

and diameter. The function $g(\alpha)$ is dimensionless. K, k_1, k_2, k_3, n_1, and n_2 are empirical model parameters; $h_v = H_v/(1\ \text{GPa})$ is dimensionless, with H_v denoting target Vickers hardness expressed as a pressure. The quantities v_0 and d_0 are the reference impact speed and particle diameter; v is the particle impact speed, d_p is particle diameter, and α is the impact angle measured from the wall tangent in radians. Particle impact speed v is distinct from inlet fluid speed U.

The Oka erosion and Forder restitution correlations were derived from controlled particle-impact experiments [10,17,18], but their experimental basis does not validate the present tool geometry. No tool-specific calibration factor was introduced. The analysis therefore emphasizes erosion location, parameter trends and relative structural differences under identical numerical settings, rather than absolute service life. Table 5 lists the Oka parameters used in the baseline and structural-comparison simulations, together with the normal-incidence volume and mass erosion ratios at the normalization conditions.

Table 5. Oka erosion-model parameters for 42CrMo steel (320 HV).

Parameter	Symbol	Parameter Value	Unit
Vickers hardness used	H_v	3.138128 (320 HV)	GPa
Dimensionless hardness used	h_v	3.138128	1
Volume erosion scale	K	65	$mm^3 \cdot kg^{-1}$
Hardness exponent	k_1	−0.12	1
Velocity exponent	k_2	2.402157	1
Diameter exponent	k_3	0.19	1
Angle exponent	n_1	0.833282	1
Angle exponent	n_2	0.819107	1
Particle-diameter normalization scale used	d_0	326	μm
Impact-speed normalization scale used	v_0	104	$m \cdot s^{-1}$
Wall density used for conversion	ρ_w	7850	$kg \cdot m^{-3}$
Normal-incidence volume ratio at normalization conditions	$E_{90,ref}$	56.664737	$mm^3 \cdot kg^{-1}$
Normal-incidence mass ratio at normalization conditions	$Y_{90,ref}$	4.448182×10^{-4}	$kg \cdot kg^{-1}$

The tabulated hardness-dependent exponents correspond to $k_2 = 2.3\ {h_v}^{0.038}$, $n_1 = 0.71\ {h_v}^{0.14}$, and $n_2 = 2.4\ {h_v}^{-0.94}$ [17,18]. The hardness conversion is 320 × 0.00980665 GPa = 3.138128 GPa, so $h_v = 3.138128$. The constants $K = 65\ mm^3 \cdot kg^{-1}$, $k_1 = -0.12$, $k_3 = 0.19$, $v_0 = 104\ m \cdot s^{-1}$, and $d_0 = 326$ μm specify the adopted correlation [17,18].

At $v = v_0$ and $d_p = d_0$, Equation (18) gives the normal-incidence volume erosion ratio $E_{90,ref} = 56.664737\ mm^3 \cdot kg^{-1}$. The corresponding mass erosion ratio is $Y_{90,ref} = 10^{-9}\ \rho_w\ E_{90,ref} = 4.448182 \times 10^{-4}\ kg \cdot kg^{-1}$. Here $\rho_w = 7850\ kg \cdot m^{-3}$ is the wall density of 42CrMo used for volume-to-mass conversion; it differs from the particle density in Section 2.6. The factor 10^{-9} converts mm^3 to m^3. For a mass-based implementation of the Oka law, $Y_{90,ref}$ is the reference erosion ratio at v_0 and d_0, while E_{90} in Equation (18) varies with the current impact speed and particle diameter.

At impact j, the wall-mass ratio is $Y_j = 10^{-9}\ \rho_w\ E_j$, where E_j is evaluated using Equations (17)–(19). The wall erosion flux is obtained by summing mass-flow-weighted impact contributions on each wall face f: $E_f = {A_f}^{-1}\ \Sigma_j\ \dot{m}_j\ Y_j$, and $E_{max} = \max_f E_f$. Here A_f is the face

area (m^2), $\dot{m}_j$ is the incident parcel mass-flow contribution ($kg \cdot s^{-1}$), and Y_j is evaluated at that collision; repeated impacts contribute separately. Therefore E_f has units of $kg \cdot m^{-2} \cdot s^{-1}$ and differs from the per-impact mass erosion ratios Y_j and $Y_{90,ref}$.

The Oka angle response was evaluated using the simulation parameters in Table 5. The angle function satisfies $g(0) = 0$ and $g(\pi/2) = 1$; its stationary maximum follows $\sin \alpha^* = n_1(1 + h_v)/[h_v(n_1 + n_2)]$, giving $\alpha^* = 41.68°$ and $g(\alpha^*) = 1.2822$. This maximum describes the oblique-impact response of the adopted angle function. All tabulated exponents are dimensionless and positive except the hardness exponent k_1.

Because downhole tool failure is usually controlled by the most severely damaged local region, the maximum erosion rate was selected as the primary evaluation index. Velocity contours, pressure contours, particle trajectories, and erosion contours were also analyzed to explain the erosion mechanism. To compare the relative variation in maximum erosion rate under different conditions, the normalized maximum erosion rate was defined as

$$\eta = \frac{E_{max,i}}{E_{max,0}} \tag{20}$$

where η is the normalized maximum erosion rate, $E_{max,i}$ is the maximum erosion rate under condition i, and $E_{max,0}$ is the maximum erosion rate under the baseline condition.

2.6. Physical Parameters and Boundary Conditions

A laboratory-prepared water-based simulated drilling fluid was used as the continuous phase, with a density of 1200 $kg \cdot m^{-3}$ and a dynamic viscosity of 0.002 Pa·s. Quartz sand particles (S861675, 120–180 mesh; Shanghai Macklin Biochemical Co., Ltd. (Macklin), Shanghai, China) were selected as the discrete phase, with a particle density of 2650 $kg \cdot m^{-3}$. The commercial sand was sieved to a characteristic diameter of approximately 100 μm for the erosion tests. The tool-wall material was 42CrMo alloy structural steel, with a nominal Vickers hardness of 320 HV (equivalent to approximately 3.14 GPa), an elastic modulus of 206 GPa, and a Poisson's ratio of 0.3. These values describe the fluid, particle, and wall-material properties.

The Vickers hardness of 320 HV was used for the Oka parameters in Table 5. The wall density of 7850 $kg \cdot m^{-3}$ converts the volume erosion ratio to a mass erosion ratio and is distinct from the quartz-particle density.

The inlet was set as a velocity inlet with a baseline inlet velocity of 15 $m \cdot s^{-1}$, an inlet turbulence intensity of 5%, and a hydraulic diameter of 76.2 mm. The outlet was set as a pressure outlet with a gauge pressure of 0 Pa. No-slip wall conditions were applied to the tool wall, guide brackets, and other solid boundaries. Particles entered the computational domain with the drilling fluid from the inlet. The baseline particle size was 100 μm, and the particle mass flow rate was 0.01 $kg \cdot s^{-1}$. Particles were assigned escape conditions at the inlet and outlet boundaries and rebound conditions at the tool wall and guide-bracket surfaces.

2.7. Sand-Laden Erosion Test and Measurement Definitions

Sand-laden tests were conducted on full-scale baseline and optimized core flow-passage assemblies made of 42CrMo steel with a nominal hardness of 320 HV. The assemblies retained the erosion-controlling flow geometry, omitted electronic components and non-flow fasteners, and used the same thread and small-chamfer simplifications as the flow model. Each geometry had three independent specimens, each weighed and scanned separately after 1800.0 s exposure. The nominal baseline test condition was 15 $m \cdot s^{-1}$ inlet velocity, 100 μm quartz sand (2650 $kg \cdot m^{-3}$) and 0.0100 $kg \cdot s^{-1}$ sand feed in fluid of density 1200 $kg \cdot m^{-3}$ and viscosity 0.002 Pa·s. New sand was metered into the loop and separated for recovery; the fluid returned to the reservoir. Each exposure used 18.000 kg sand.

The tests used a custom-built closed-loop solid–liquid two-phase erosion rig comprising a circulation pump, a quantitative sand feeder, a specimen-mounting section, a solid–liquid separator and a liquid reservoir. Carrier fluid was driven by a D155-30 × 10 multistage centrifugal pump (Changsha Zoomlian Pump Co., Ltd., Changsha, China). Flow measurement used a ProcessMaster FEP630 electromagnetic flowmeter (ABB Automation Products GmbH, Göttingen, Germany). Pressure measurement used the A-10 pressure transmitter (WIKA Alexander Wiegand SE & Co. KG, Klingenberg, Germany), with an actual measurement range of 0–10 MPa. Figure 4 presents a functional conceptual schematic of carrier-fluid circulation, sand injection and recovery. In the schematic, the pump supplies carrier fluid from the reservoir through the flowmeter, and fresh sand enters upstream of the test section. The mixture passes around the guide hood, through the annular passage and past the bracket-root regions. Downstream separation directs sand to recovery and returns the carrier fluid to the reservoir. The inlet and outlet pressure positions identify the boundaries for evaluating pressure drop across the test section, while panel (b) shows the core assembly and inspection regions. Equipment order and pressure positions are illustrative, and the schematic is not to scale.

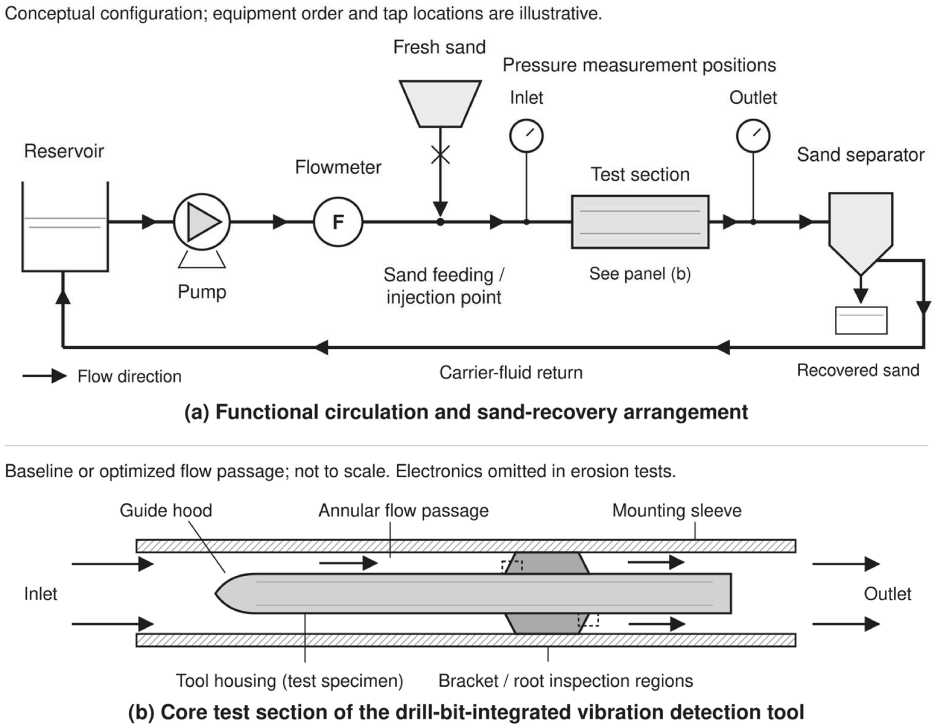


Figure 4. Conceptual schematic of the sand-laden erosion loop.

The inlet velocity was defined on the unobstructed annular section upstream of the brackets, with sleeve inner diameter 69.2 mm and tool outer diameter 48 mm. Its area was 0.00195143 m^2, giving 0.02927148 $m^3 \cdot s^{-1}$ (1756.29 $L \cdot min^{-1}$) at 15 $m \cdot s^{-1}$. The inlet-velocity check range was 15.00 ± 0.08 $m \cdot s^{-1}$. The 76.2 mm hydraulic-diameter input in Section 2.6 is the numerical turbulence-boundary setting; it is not used to calculate this annular area.

After erosion exposure, specimens were initially cleaned with analytical-grade anhydrous ethanol (AR, product No. 10009218; Sinopharm Chemical Reagent Co., Ltd., Shanghai, China), rinsed with deionized water, dried at 60 °C for 60 min and rested for 30 min. The pressure housing, bracket assembly and sleeve were weighed separately using an XPR3003S high-precision electronic balance (Mettler-Toledo (Schweiz) GmbH, Greifensee, Switzerland; maximum capacity, 3.1 kg; readability, 1 mg), and their masses were summed; each part weighed less than 3.1 kg. Three no-sand blanks followed the same

exposure time and cleaning/drying procedure and gave a mean apparent loss of 0.002 g. The net mass loss Δm was calculated by subtracting the summed post-exposure masses and the mean blank loss of 0.002 g from the summed pre-exposure masses; the overall mass-loss rate is Δm/t. Repeated weighing does not increase the number of independent specimens.

Three-dimensional surface topography was measured using a VR-6000 Series 3D Optical Profiling System (KEYENCE CORPORATION, Osaka, Japan), equipped with a VR-6200 automatic scanning head and a VR-H4J measurement extension module. Pre- and post-exposure surface scans had 1 μm vertical and 10 μm lateral resolution and were registered to protected reference lands. Multi-field stitching covered the full 70 mm bracket and both root-transition regions. Local depth change Δh was averaged over a registered 0.20 × 0.20 mm window. The local depth rate is Δh/t, and the equivalent local mass flux is $\rho_w \Delta h$/t, with Δh in meters and $\rho_w = 7850$ kg·m^{-3}. The corresponding weighed wall areas were 0.1180 m^2 (baseline) and 0.1120 m^2 (optimized). Whole-assembly loss is compared with the CFD wall-area integral (mean flux multiplied by the corresponding area); local converted flux is compared with the same-scale CFD matched window, rather than a single-face maximum.

We report experimental results as the mean and sample standard deviation (SD, denominator $n - 1$) of three independent specimens per geometry. The experimental error bars show this SD, while the DPM bars show observed minimum–maximum ranges. The Type A standard uncertainty of a group mean is SD/$\sqrt{3}$. For the mass-loss budget, we combined SD/$\sqrt{3}$ in quadrature with a 1.000 mg Type B contribution to each group mean and a 0.5774 mg blank-mean contribution. This calculation gives combined standard uncertainties of 3.4157 and 2.1082 mg for the baseline and optimized geometries, respectively [31].

The 1 mg balance increment describes readout resolution and is distinct from the standard-uncertainty components used in the budget. Our mass-loss measurement model includes the pre- and post-exposure readings for the pressure housing, bracket assembly and sleeve, together with the blank correction. The cleaning and drying procedure and the no-sand blanks address handling and residue effects in this measurement chain. Because both geometry means use the same blank correction, their mass losses share a covariance term.

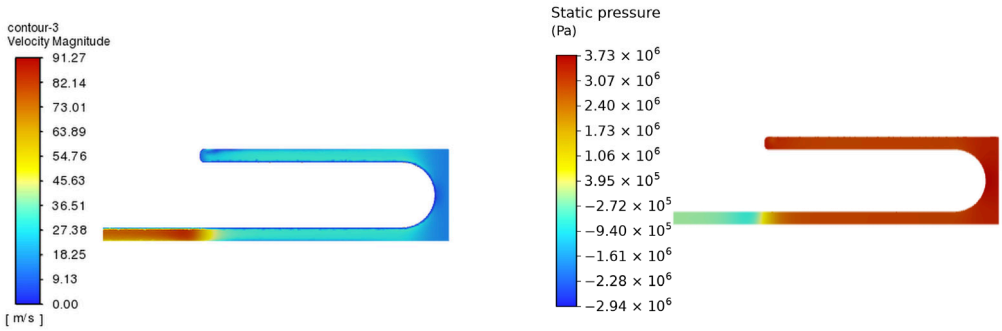
We used a time resolution of 0.1 s and a uniform rounding-error model, giving a time standard uncertainty of 0.02887 s. The Type B contribution assigned to local depth was 1.08012 μm. We distinguish this budget component from the vertical and lateral scan resolutions. Local depth is defined by the difference between the registered pre- and post-exposure surfaces, so registration, the reference surface and the averaging window are part of the measurement definition.

We express the derived erosion quantities as Δm/t, Δh/t and $\rho_w \Delta h$/t. First-order GUM propagation relates their standard uncertainties to the sensitivity coefficients and covariances of the input quantities [31]. The mass-loss rate depends on mass and time, the depth rate on depth and time, and the converted local flux additionally on wall density. For optimized-to-baseline ratios, we distinguish the independent-specimen repeatability contribution reported in Section 3.5 from shared-correction and Type B terms in the measurement model. We report standard uncertainties at $k = 1$; these are distinct from sample SD and from 95% coverage intervals. The available budget does not quantify every input contribution, including wall-density uncertainty; the converted local fluxes are therefore reported using the adopted density.

3. Results

3.1. Baseline-Structure Flow-Field Distribution Characteristics

The velocity and pressure contours of the baseline structure are shown in Figure 5. The drilling fluid experiences guide-hood diversion, annular-channel bypass flow, inter-bracket flow, and downstream discharge. Thus, both the flow direction and the local cross-sectional area change. Figure 5a shows that the drilling fluid enters the upper flow passage and remains relatively stable, with limited variation in the main-flow velocity. When the fluid reaches the right closed end and turning region, the flow direction changes markedly because of wall obstruction and flow-path geometry, and a low-speed stagnation zone forms locally. Figure 5b shows that part of the fluid kinetic energy is converted into pressure energy in this region, producing a local high-pressure zone with a maximum pressure of approximately 3.7 MPa.



(**a**) (**b**)

Figure 5. Internal velocity and pressure fields of the baseline structure: (**a**) velocity contour; (**b**) pressure contour.

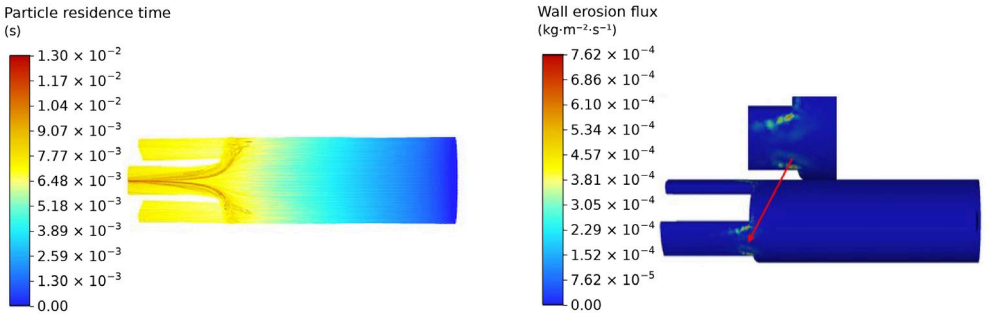
When the drilling fluid further turns back and enters the lower outlet channel, the local flow area decreases and a strong pressure gradient develops. Therefore, the flow accelerates through the channel transition, and the local maximum velocity reaches approximately 91.27 m·s^{-1}. This high-velocity region is concentrated near the abrupt contraction, brackets, and outlet transition. Higher local flow speed can increase particle impact energy; the actual erosion response also depends on particle slip, impact angle and wall-impact loading.

The pressure distribution shows a distinct high-pressure region at the closed end and turning region, followed by a gradual pressure decrease toward the outlet. The pressure gradient accelerates the fluid in the downstream narrow channel and enhances the directional motion of particles. Because solid particles are much denser than the drilling fluid, they cannot immediately follow the sharply changing streamlines and tend to deviate from the main flow and collide with the wall owing to inertia. Therefore, local acceleration, pressure concentration, and streamline deflection in the baseline flow field provide a plausible fluid-dynamic explanation for the subsequent particle-trajectory deviation and erosion concentration.

These fields indicate a geometry-dependent flow rather than uniform annular flow. Erosion interpretation therefore combines velocity, pressure, particle trajectories and wall flux. Figures 1 and 4 explain installation and test-loop functions, whereas the selected computed views show flow fields, particle trajectories and wall erosion. These views do not provide a dimensioned registration between the test assembly and CFD faces. Comparisons in Section 3.5 are consequently conditional on consistent inlet-section, exposed-wall and local-window definitions.

3.2. Particle Trajectories and Erosion-Concentration Zones

The particle trajectories and wall erosion contours of the baseline structure are shown in Figure 6. Solid particles enter the computational domain with the drilling fluid, first bypass the tool head under the action of the guide hood, and then enter the annular channel. No large-area severe erosion occurs at the front end of the guide hood, indicating that it can reduce direct frontal particle impact to some extent. However, after particles enter the channel transition and bracket region, their trajectories undergo pronounced deflection. Some particles deviate from the main-flow direction under inertial effects and move toward the wall.



(**a**) (**b**)

Figure 6. Particle trajectory and erosion contour of the baseline structure: (**a**) particle trajectory; (**b**) erosion contour. Colors denote particle residence time in (**a**) and wall erosion flux in (**b**). The red arrow links the enlarged view to the corresponding bracket-root erosion region.

Erosion damage in the baseline structure is strongly localized, with the most severe erosion concentrated near the channel transition and guide-bracket roots. This region corresponds to the local high-velocity zone in the velocity contour, the particle-deflection concentration zone in the particle trajectory, and the geometric discontinuity in the structure. The spatial correspondence is consistent with a combined influence of impact speed, erosion-favorable impact angle, and concentrated wall-impact loading. The maximum erosion rate of the baseline structure is 7.62×10^{-4} kg·m^{-2}·s^{-1}, and the maximum particle residence time is approximately 1.30×10^{-2} s.

The axial erosion distribution has a localized peak, indicating geometry-controlled wear rather than uniform wall loss. Increasing wall thickness or hardness alone does not remove the cause of concentrated impacts. Structural changes should instead reduce the combined mass-weighted erosion response by modifying impact speed, the angle distribution, and wall-impact loading. Because the Oka angle function is non-monotonic, a smaller impact angle is not by itself evidence of lower erosion.

3.3. Effects of Particle Parameters on Erosion Behavior

The erosion behavior of the drill-bit-integrated vibration detection tool is affected not only by the local flow-field structure, but also by the characteristics of the solid particles carried by the drilling fluid. Among these factors, inlet velocity, particle size, and particle mass flow rate directly influence particle kinetic energy, flow-following ability, wall-impact frequency, and impact position. Therefore, based on the baseline structure, the effects of these three particle parameters on the maximum erosion rate were investigated using the controlled-variable method. During each group of simulations, only one parameter was changed, while the material properties, boundary conditions, turbulence model, DPM settings, particle rebound model, and erosion model were kept unchanged.

The following subsections present all simulated parameter cases and representative erosion contours; the selected contour conditions are specified in Section 3.3.4.

In the parameter-response plots, markers show production-grid values and asymmetric bars span each center and five DPM repeats (Tables 3 and 4); B0 is shared across the figures. The bars describe the recorded minimum–maximum spread at fixed carrier-phase conditions. They are not SD, confidence intervals, significance tests or total-error bounds. Non-overlap indicates separation within the recorded spread; overlap alone does not establish equivalence.

3.3.1. Effect of Inlet Velocity

With the particle size fixed at 100 μm and the particle mass flow rate fixed at 0.01 kg·s^{-1}, inlet velocities of 5, 10, 15, 20, and 25 m·s^{-1} were selected. The corresponding maximum erosion rates are listed in Table 6.

Table 6. Maximum erosion rate under different inlet velocities.

Inlet Velocity, U (m·s^{-1})	Maximum Erosion Rate, E_{max} (kg·m^{-2}·s^{-1})
5	5.70×10^{-5}
10	2.81×10^{-4}
15	7.62×10^{-4}
20	1.96×10^{-3}
25	2.92×10^{-3}

Figure 7 shows a marked increase in maximum erosion rate with inlet velocity. The observed minimum–maximum ranges at successive velocities do not overlap, and the increasing response persists across the repeat-to-repeat spread.

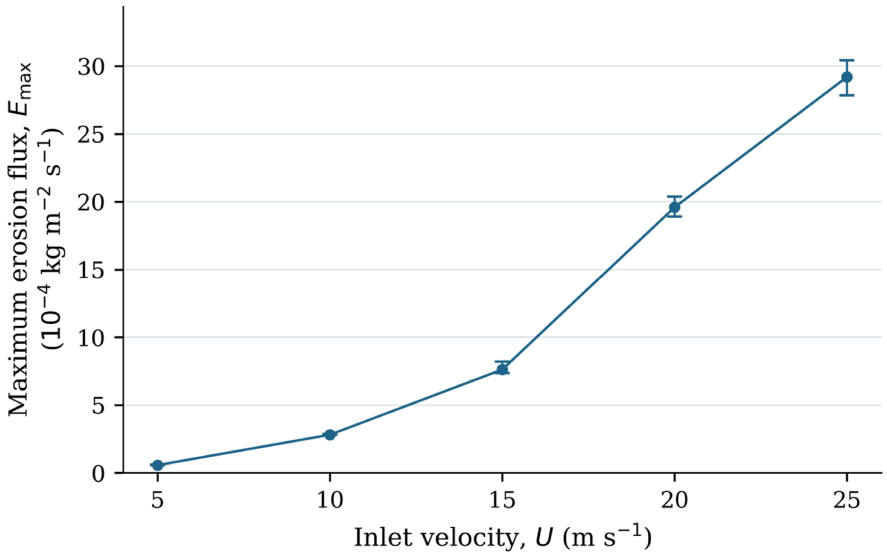


Figure 7. Variation in maximum erosion rate with inlet velocity. Markers are production-grid values; bars span the observed minimum–maximum limits across each marker and five DPM repeats (Tables 3 and 4), not total uncertainty.

The dependence of maximum erosion rate on inlet velocity is consistent with velocity-sensitive erosion behavior. According to the Oka erosion model and solid-particle erosion theory, particle impact velocity usually influences material removal rate through a power-law relationship. As inlet velocity increases, particles acquire greater kinetic energy in the flow field and more readily penetrate the near-wall low-speed region before impacting the

wall. Local channel contraction further amplifies this velocity effect, causing concentrated high-energy impacts at the bracket roots and transition region.

From an engineering perspective, when the inlet velocity increases from 5 to 25 $m \cdot s^{-1}$, the maximum erosion rate increases from 5.70×10^{-5} to 2.92×10^{-3} $kg \cdot m^{-2} \cdot s^{-1}$, corresponding to a factor of approximately 51.2 between the lowest and highest tested cases. Thus, within the investigated ranges, inlet velocity produces the largest change in predicted erosion rate among the three parameters considered. For a drill-bit-integrated vibration detection tool, practical design should not only consider the total drilling-fluid displacement, but also focus on throttling acceleration in local flow passages. If the local structure causes a sudden reduction in flow area, local high-velocity erosion risk may still form near the bracket roots or outlet transition region even when the average inlet velocity is not high.

3.3.2. Effect of Particle Size

At an inlet velocity of 15 $m \cdot s^{-1}$ and a particle mass flow rate of 0.01 $kg \cdot s^{-1}$, particle sizes of 100, 200, 300, and 400 μm were selected to investigate the influence of particle size on wall erosion. The corresponding maximum erosion rates are shown in Table 7.

Table 7. Maximum erosion rate at different particle sizes.

Particle Size, d_p (μm)	Maximum Erosion Rate, E_{max} ($kg \cdot m^{-2} \cdot s^{-1}$)
100	7.62×10^{-4}
200	1.85×10^{-3}
300	1.36×10^{-3}
400	1.33×10^{-3}

Figure 8 shows the particle-size response listed in Table 7.

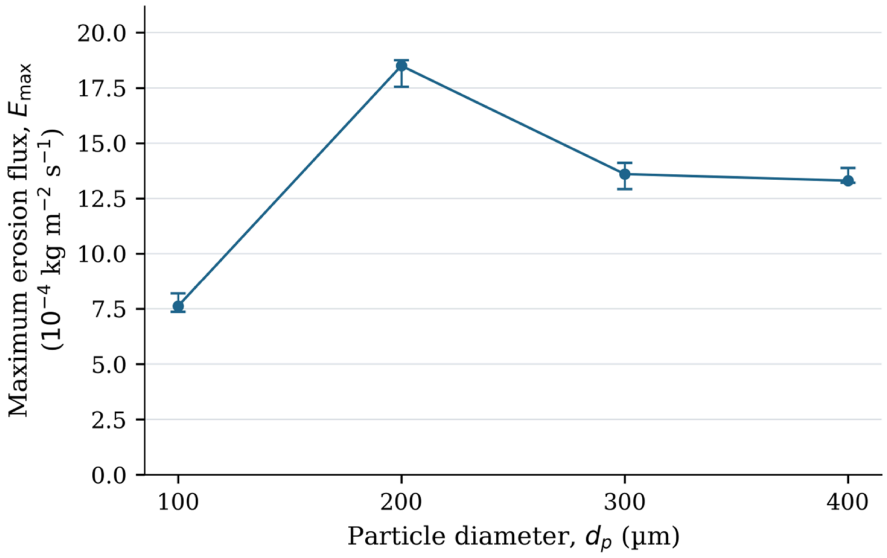


Figure 8. Variation in maximum erosion rate with particle size. Markers are production-grid values; bars span the observed minimum–maximum limits across each marker and five DPM repeats (Tables 3 and 4), not total uncertainty.

Among the four tested sizes, 200 μm gives the largest predicted maximum erosion rate, 1.85×10^{-3} $kg \cdot m^{-2} \cdot s^{-1}$. The 300 and 400 μm values are lower, but their recorded ranges overlap: 12.9148–14.1123 and 13.2035–13.8758, respectively, in 10^{-4} $kg \cdot m^{-2} \cdot s^{-1}$. Thus, the data resolve a non-monotonic response over 100–400 μm without establishing a stable ordering between 300 and 400 μm or the exact peak diameter.

Greater particle inertia may explain the increase from 100 to 200 µm by weakening flow following near sharply turning streamlines. At fixed sand mass flow, particle number flux decreases with diameter, but DPM erosion is mass-flow weighted, so the particle number alone cannot explain the subsequent decline. Changes in impact speed, angle and wall-impaction efficiency may contribute. Simulations at intermediate sizes and wall-impact statistics are needed to distinguish these effects and locate the peak.

3.3.3. Effect of Particle Mass Flow Rate

At an inlet velocity of 15 m·s^{-1} and a particle size of 100 µm, particle mass flow rates of 0.005, 0.010, 0.015, 0.020, and 0.025 kg·s^{-1} were selected. The corresponding maximum erosion rates are shown in Table 8.

Table 8. Maximum erosion rate under different particle mass flow rates.

Particle Mass Flow Rate, q_m (kg·s^{-1})	Maximum Erosion Rate, E_{max} (kg·m^{-2}·s^{-1})
0.005	3.56×10^{-4}
0.010	7.62×10^{-4}
0.015	1.07×10^{-3}
0.020	1.43×10^{-3}
0.025	1.78×10^{-3}

Figure 9 shows increasing maximum erosion rate with particle mass flow rate. The observed minimum–maximum ranges at successive settings do not overlap, and the increasing response persists across the repeat-to-repeat spread.

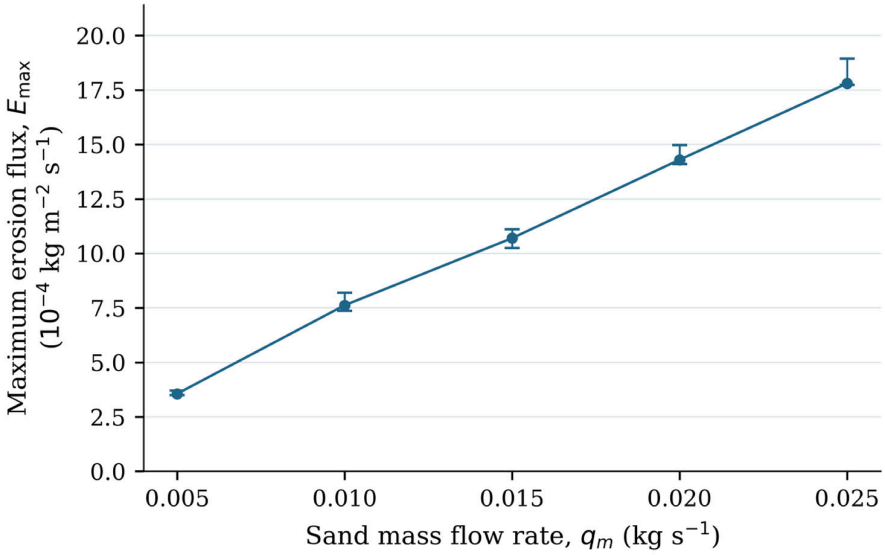


Figure 9. Variation in maximum erosion rate with particle mass flow rate. Markers are production-grid values; bars span the observed minimum–maximum limits across each marker and five DPM repeats (Tables 3 and 4), not total uncertainty.

At fixed inlet velocity and monodisperse particle size, increasing sand mass flow increases particle mass and number fluxes, while the characteristic single-particle impact energy remains governed by the flow and particle size. The maximum erosion rate rises approximately fivefold, from 3.56×10^{-4} to 1.78×10^{-3} kg·m^{-2}·s^{-1}, as sand mass flow increases from 0.005 to 0.025 kg·s^{-1}, consistent with increased wall-impact loading.

The approximately proportional response depends on the flow and impact trajectories per unit injected particle mass. Wall-impact statistics are needed to explain departures from strict proportionality.

3.3.4. Representative Wall Erosion-Rate Distributions

Figure 10 compares representative contours at 5, 15 and 25 m·s^{-1}; 100, 200 and 400 µm; and 0.005, 0.015 and 0.025 kg·s^{-1}. All cases remain in Tables 6–8. Separate scales resolve patterns within each case; identical colors do not indicate equal absolute flux. The same limitation applies to the other separately scaled contour comparisons below. Absolute peaks are compared using the corresponding tables.

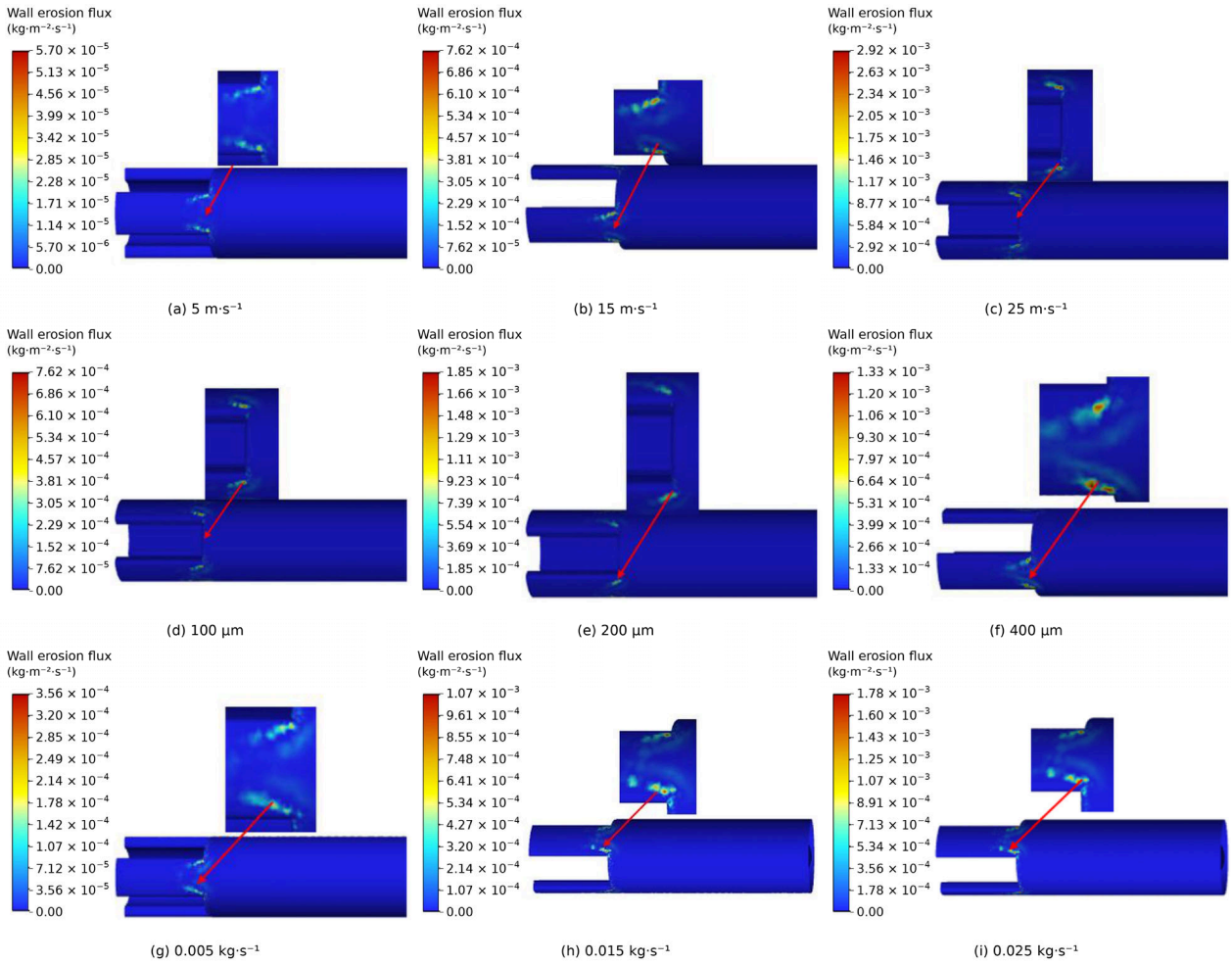


Figure 10. Representative wall erosion-rate distributions under selected particle-parameter conditions: (**a**) 5 m·s^{-1}, (**b**) 15 m·s^{-1}, and (**c**) 25 m·s^{-1}; (**d**) 100 µm, (**e**) 200 µm, and (**f**) 400 µm; (**g**) 0.005 kg·s^{-1}, (**h**) 0.015 kg·s^{-1}, (**i**) 0.025 kg·s^{-1}. Each panel uses a separate color-scale range. Red arrows link enlarged views to the corresponding bracket-root regions in the main views.

The comparison shows that the high-erosion regions under different particle parameters are generally concentrated near the channel transition and guide-bracket roots. This is consistent with the baseline erosion analysis, indicating that the local structural geometry determines the main erosion-prone positions. However, different particle parameters change the erosion intensity and the distribution range of the high-erosion region. Inlet velocity produces the largest response range and strongly amplifies the local erosion peak. Particle size changes particle inertia, flow-following behavior, and wall-impact characteris-

tics, resulting in a non-monotonic erosion response. Particle mass flow rate mainly increases particle mass loading and wall-impact loading at the existing high-risk regions.

3.3.5. Comparison of Parameter-Response Ranges

Equation (20) defines the maximum erosion rate relative to the baseline condition. For a compact cross-parameter summary, the response range within each one-factor series was additionally described by the ratio $E_{max,max}/E_{max,min}$. The baseline condition corresponds to an inlet velocity of 15 m·s^{-1}, a particle size of 100 µm, and a particle mass flow rate of 0.01 kg·s^{-1}. The resulting response-range comparison is shown in Figure 11.

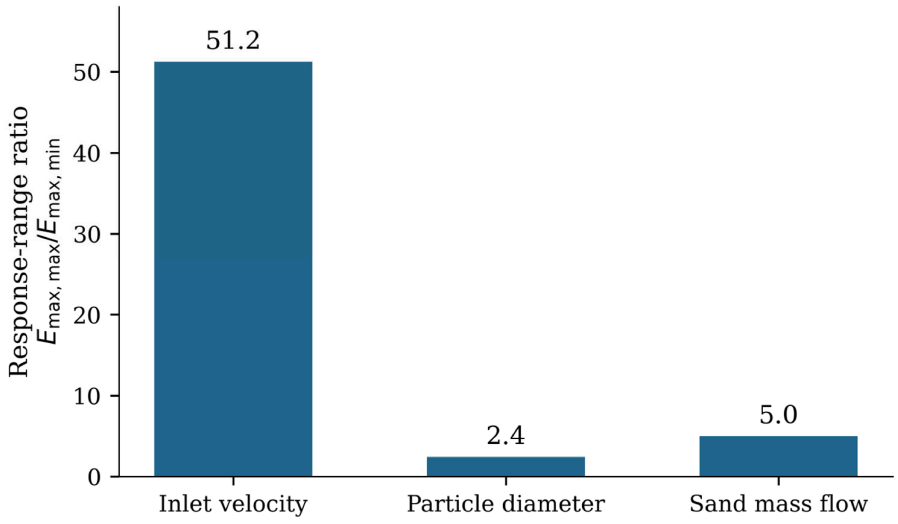


Figure 11. Range ratio of maximum erosion rate across the investigated parameter ranges.

Across the investigated one-factor ranges, the ratio $E_{max,max}/E_{max,min}$ is 51.2 for inlet velocity, 2.4 for particle size, and 5.0 for particle mass flow rate. These values are descriptive response-range ratios rather than formal normalized sensitivity coefficients, because the three input parameters were varied over different physical intervals. Even with this limitation, inlet velocity produces the largest variation in predicted E_{max} over the tested ranges. Particle mass flow rate primarily scales particle–wall-impact loading, whereas particle size changes particle inertia, flow-following behavior, and wall-impact statistics; accordingly, the particle-size response is non-monotonic in the present geometry.

The following empirical relation was reported for the baseline geometry with a hemispherical guide hood, three brackets and a 3 mm root fillet, under the properties and numerical settings in Sections 2.2–2.6:

$$E_{max} = q_m \cdot U^n \left(A{d_p}^2 + B d_p + C \right) \quad (21)$$

where E_{max} is the maximum wall erosion rate, q_m is particle mass flow rate in kg·s^{-1}, U is inlet fluid speed in m·s^{-1}, and d_p is particle diameter in m. The reported coefficients are $A = -21328.55$, $B = 11.959$, $C = -5.530 \times 10^{-4}$, and $n = 2.213$, with $R^2 = 0.8301$ and adjusted $R^2 = 0.8281$. To return E_{max} in kg·m^{-2}·s^{-1}, A, B, and C have units s^n·m$^{-(n+4)}$, s^n·m$^{-(n+3)}$, and s^n·m$^{-(n+2)}$, respectively.

Our one-factor studies cover inlet velocities of 5–25 m·s^{-1}, particle diameters of 100–400 µm and particle mass flow rates of 0.005–0.025 kg·s^{-1}. We held the other inputs at 15 m·s^{-1}, 100 µm and 0.01 kg·s^{-1}, as applicable. The reported coefficients require particle diameter in meters.

We use Equation (21) to summarize the fitted simulation data. The one-factor studies do not validate all combinations within these ranges. We require additional validation and,

where necessary, refitting for untested combinations, conditions outside these ranges, other geometries including the optimized structure, or changes in fluid, particle or wall-material properties. The Oka parameters in Table 5 were specified separately as simulation inputs. The case-by-case simulation values in Tables 6–8 and the associated erosion contours were used for the subsequent structural comparison.

The response-range comparison is conditional on the investigated intervals and baseline geometry. It does not establish a universal ranking of parameter importance. The response-range ratios summarize the changes in the simulated maximum erosion rate over the selected operating intervals.

3.4. Erosion-Resistant Structural Optimization

3.4.1. Optimization Objectives

The baseline analysis locates the main erosion zones at the channel transition and bracket roots, where local acceleration, streamline deflection, and repeated impacts may interact. Structural optimization therefore targets the combined mass-weighted wall-impact response through changes in the flow passage and particle trajectories. Neither a lower fluid-velocity maximum nor a smaller impact angle alone is a sufficient erosion criterion.

The guide-hood shape, number of guide brackets, and bracket-root fillet radius were selected as optimization variables. The guide-hood shape mainly affects flow-direction change and initial particle deflection when drilling fluid enters the annular channel. The bracket number affects annular-channel division, bracket frontal area, and particle collision probability. The bracket-root fillet radius affects local transition continuity, near-wall streamline deflection, and high-angle particle impact. The maximum erosion rate was used as the main optimization indicator, and velocity distribution, particle trajectory, high-erosion-zone range, and pressure-drop variation were also considered.

3.4.2. Guide-Hood Structure Optimization

To analyze the influence of guide-hood shape, five structures were designed under the same inlet diameter, outlet expansion size, material parameters, and boundary conditions: a 30° semi-conical shape, a 45° semi-conical shape, a 1.5:1 elliptical shape, a 2:1 elliptical shape, and the original hemispherical shape. These structures are shown in Figure 12.

Wall erosion contours for the five schemes were compared under the same boundary conditions and particle parameters, as shown in Figure 13. The corresponding maximum erosion rates are listed in Table 9. We use the separately scaled contours to identify hotspots and spatial patterns within each case. Identical colors across panels do not indicate equal absolute erosion rates; we compare absolute peaks using Table 9.

Table 9. Maximum erosion rate of different guide-hood structures.

Guide-Hood Structure	Maximum Erosion Rate, E_{max} ($kg \cdot m^{-2} \cdot s^{-1}$)
30° semi-conical	1.01×10^{-3}
45° semi-conical	6.49×10^{-4}
1.5:1 elliptical	1.03×10^{-3}
2:1 elliptical	8.48×10^{-4}
Original hemispherical	7.62×10^{-4}

The erosion results of different guide-hood structures show that the guide-hood shape has a substantial influence on the maximum erosion rate. However, a smoother profile does not necessarily lead to a lower erosion rate. Although the 30° semi-conical guide hood provides a relatively long guiding transition, it may cause particles to form a more

concentrated deflection path when entering the annular flow channel, resulting in high-energy impacts near the downstream guide brackets. Similarly, the 1.5:1 elliptical guide hood may change the particle impact angle in the downstream flow passage and promote local particle accumulation near the bracket roots or channel transition region. As a result, its maximum erosion rate is even higher than that of the original hemispherical structure.

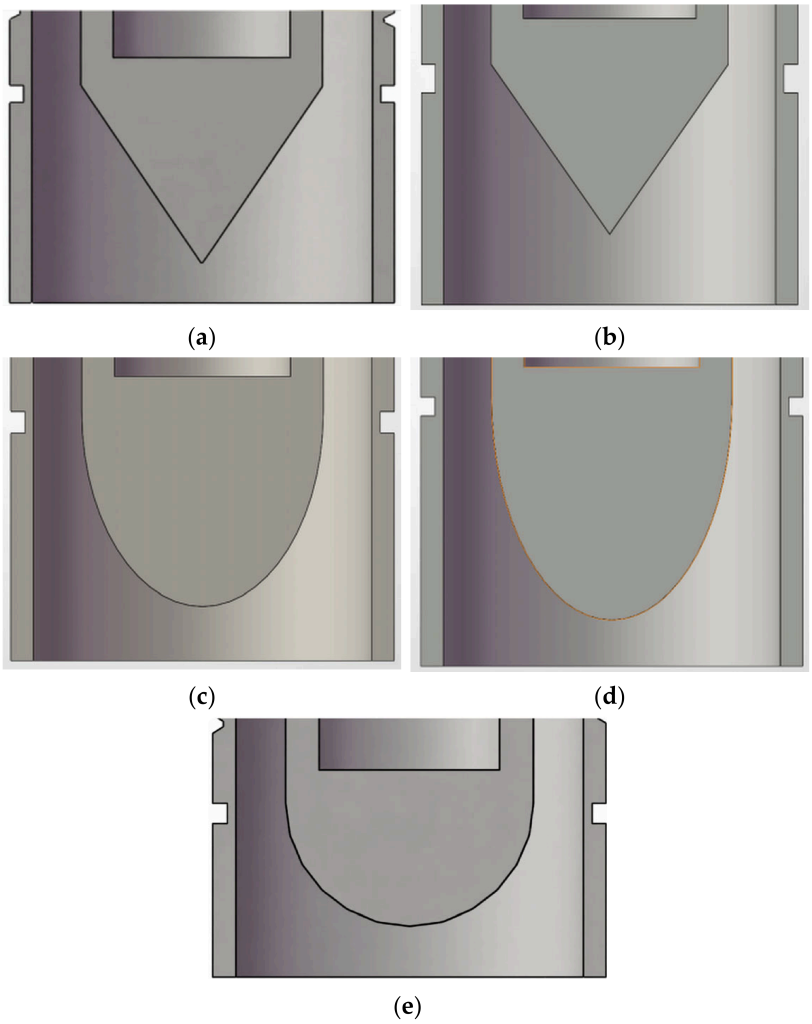


Figure 12. Different guide-hood structures: (**a**) 30° semi-conical; (**b**) 45° semi-conical; (**c**) 1.5:1 elliptical; (**d**) 2:1 elliptical; (**e**) hemispherical.

In contrast, the 45° semi-conical guide hood achieves a better balance between guiding length and flow-deflection intensity. This structure can prevent the drilling fluid and particles from directly impacting the upstream end of the tool, while avoiding excessive particle concentration near the bracket-root region. Therefore, the probability of local high-energy particle impacts is reduced. The simulation results show that the maximum erosion rate of the 45° semi-conical guide hood is 6.49×10^{-4} kg·m^{-2}·s^{-1}, which is approximately 14.8% lower than that of the original hemispherical guide hood, indicating better erosion resistance.

For ductile materials such as the 42CrMo alloy steel, erosion damage is strongly related to particle impact angle. Some guide-hood shapes may improve streamline continuity but cause particles to impact downstream walls at angles more favorable for micro-cutting and plowing. Therefore, the guide hood should be designed not only to divert the main flow, but also to control the downstream particle-impact path and avoid particle concentration

near the bracket roots. Based on the above comparison, the 45° semi-conical guide hood was selected as the preferred structure.

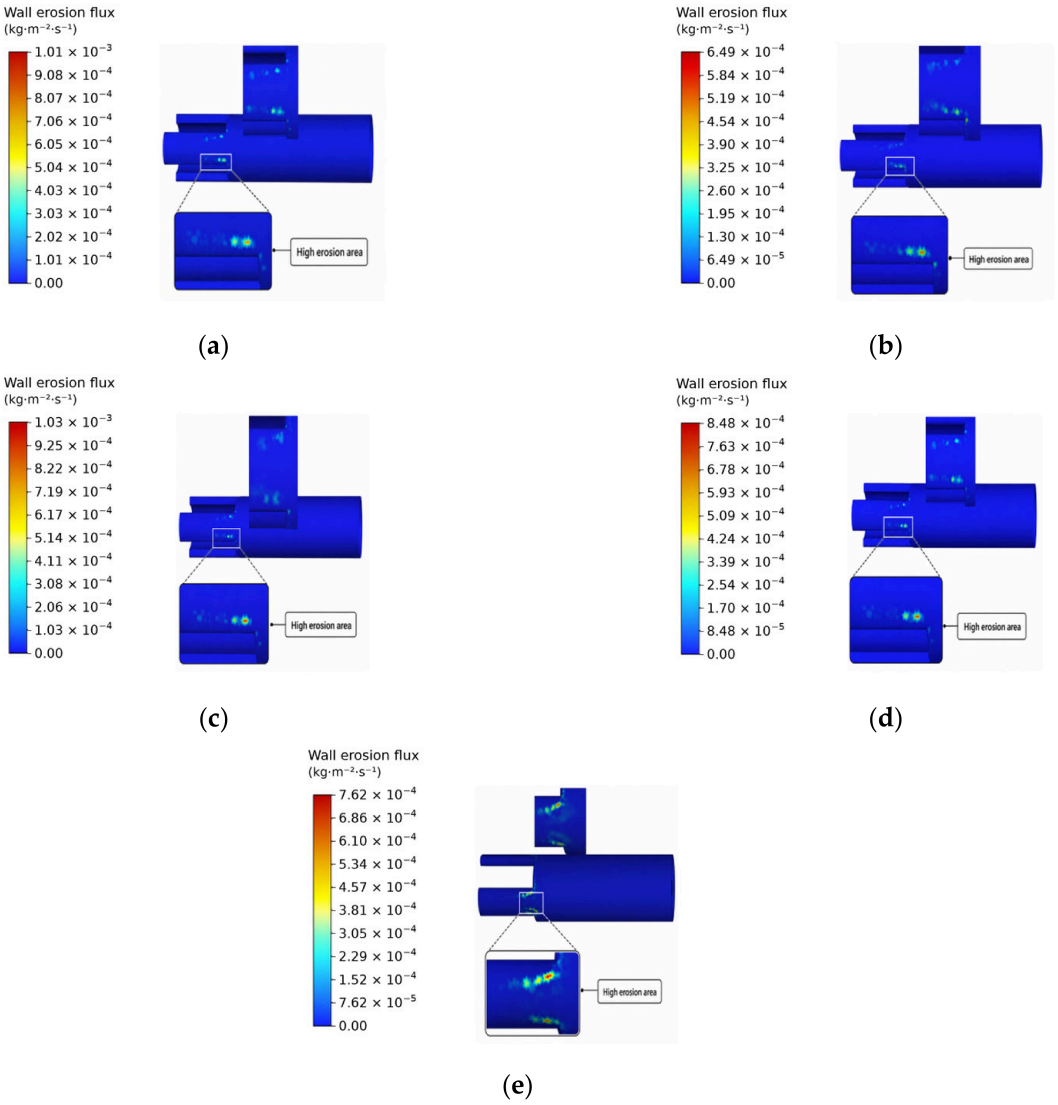
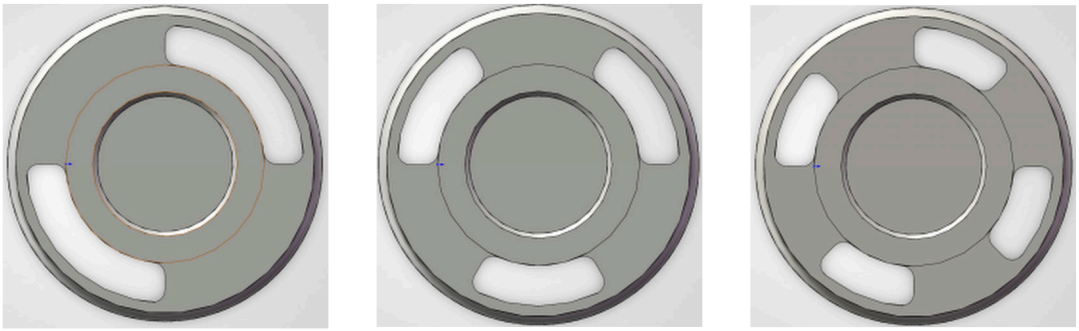


Figure 13. Wall erosion contours under different guide-hood structures: (**a**) 30° semi-conical; (**b**) 45° semi-conical; (**c**) 1.5:1 elliptical; (**d**) 2:1 elliptical; (**e**) hemispherical. Each panel uses a separate color-scale range. Outlined windows and dashed connectors identify enlarged high-erosion regions.

3.4.3. Guide Bracket Number Optimization

The guide brackets connect the tool body to the external sleeve and divide the annular channel. Two-wing, three-wing, and four-wing models were compared, as shown in Figure 14. The comparison maintained the bracket cross-sectional form, bracket-root fillet, overall supporting cross-sectional area, and numerical settings while changing the circumferential bracket number. We used this series to compare erosion responses with the total supporting area retained as a geometric constraint. This constraint does not establish equivalent directional stiffness, load-dependent centering accuracy or fatigue resistance among the layouts.



(**a**) (**b**) (**c**)

Figure 14. Structures with different numbers of guide brackets: (**a**) two-wing bracket; (**b**) three-wing bracket; (**c**) four-wing bracket.

Under the same inlet velocity, particle size, and particle mass flow rate, erosion simulations were performed for the different bracket-number schemes. The maximum erosion rates are shown in Table 10 and Figure 15.

Table 10. Maximum erosion rate under different numbers of guide brackets.

Number of Guide Brackets	Maximum Erosion Rate, E_{max} ($kg \cdot m^{-2} \cdot s^{-1}$)
Two-wing bracket	6.42×10^{-4}
Three-wing bracket	6.71×10^{-4}
Four-wing bracket	9.65×10^{-4}

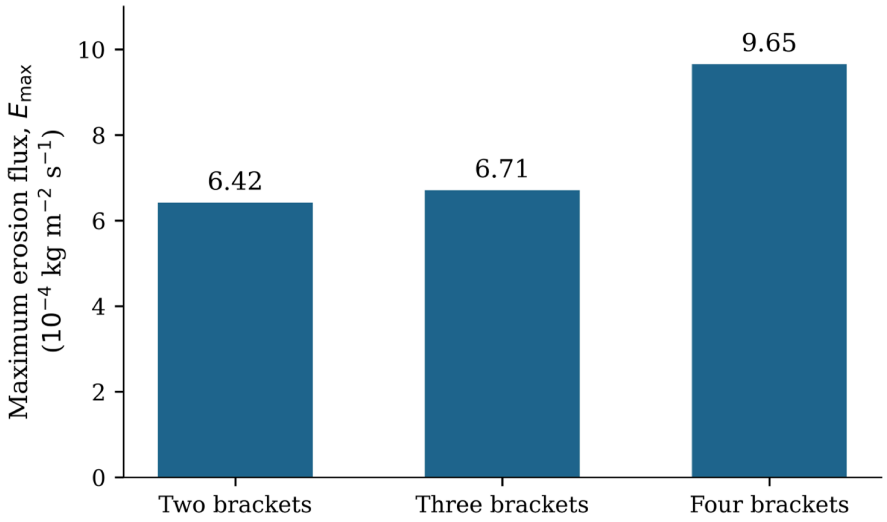


Figure 15. Comparison of maximum erosion rates for different numbers of guide brackets.

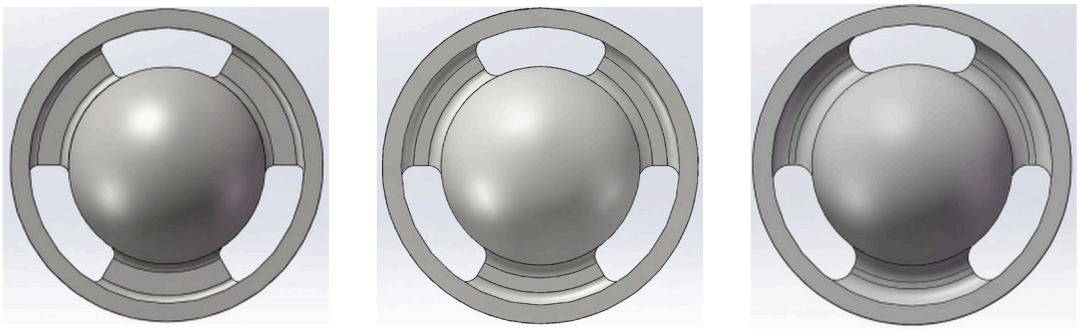
Within the bracket-number series in Table 10, the two-wing layout gives the lowest maximum erosion rate, 6.42×10^{-4} $kg \cdot m^{-2} \cdot s^{-1}$; the three-wing and four-wing values are 6.71×10^{-4} and 9.65×10^{-4} $kg \cdot m^{-2} \cdot s^{-1}$, respectively. The two-wing result is approximately 4.3% below the three-wing result and 33.5% below the four-wing result. Changes in passage subdivision and secondary rebound provide a physical explanation for the differences in the predicted erosion response. We selected the two-wing layout as the preferred scheme for erosion mitigation within this series. These percentages are not independent additive contributions to the final baseline-to-optimized reduction.

The bracket-number series uses its three-wing case ($E_{max} = 6.71 \times 10^{-4}$ $kg \cdot m^{-2} \cdot s^{-1}$) as the comparison condition. The final assessment in Section 3.4.5 instead uses the hemispher-

ical, three-wing, 3 mm baseline (7.62×10^{-4} kg·m^{-2}·s^{-1}); each percentage is calculated against its corresponding comparison condition.

3.4.4. Bracket-Root Fillet Optimization

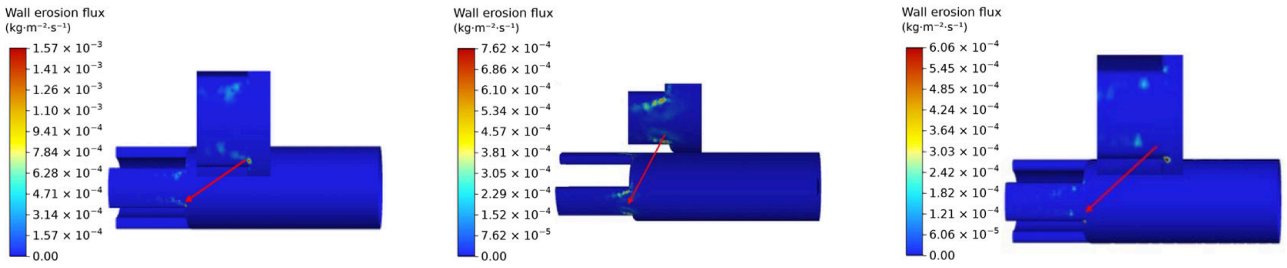
The bracket root and channel transition are the main erosion-concentration regions in the baseline structure. A sharp transition can cause boundary-layer separation, local vortices, and high-angle particle impact. Increasing fillet radius changes transition continuity and may alter local separation and particle impacts. To analyze the influence of bracket-root fillet radius, three radii, 2, 3, and 4 mm, were compared, as shown in Figure 16.



(**a**) (**b**) (**c**)

Figure 16. Structures with different bracket-root fillet radii: (**a**) 2 mm fillet; (**b**) 3 mm fillet; (**c**) 4 mm fillet.

The wall erosion distributions for different fillet radii are compared in Figure 17, and the corresponding maximum erosion rates are shown in Table 11. We use the separately scaled contours to identify local erosion patterns; identical colors across panels do not indicate equal absolute erosion rates. We compare absolute peaks using Table 11.



(**a**) (**b**) (**c**)

Figure 17. Wall erosion contours under different fillet radii: (**a**) 2 mm fillet; (**b**) 3 mm fillet; (**c**) 4 mm fillet. Each panel uses a separate color-scale range. Red arrows link enlarged views to the corresponding bracket-root erosion regions.

Table 11. Maximum erosion rate under different fillet radii.

Fillet Radius, R (mm)	Maximum Erosion Rate, E_{max} (kg·m^{-2}·s^{-1})
2	1.57×10^{-3}
3	7.62×10^{-4}
4	6.06×10^{-4}

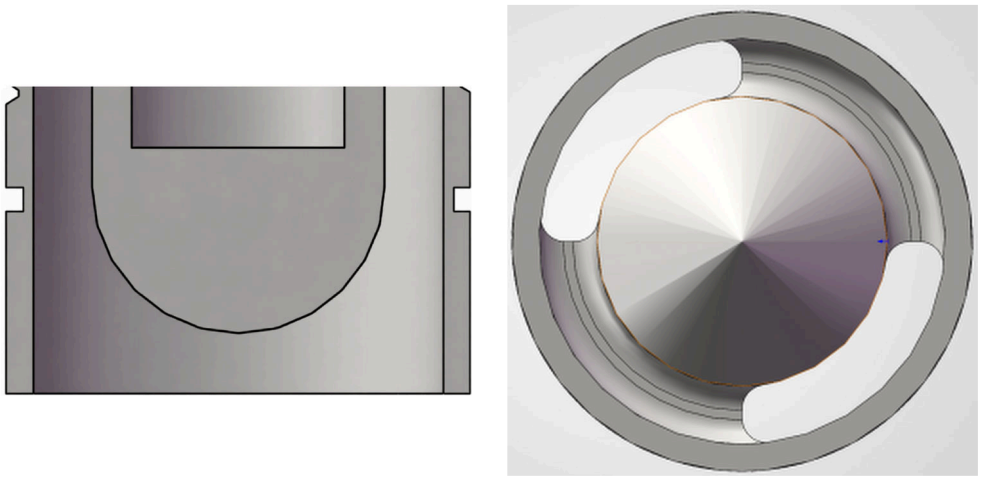
The comparison results show that the bracket-root fillet radius directly affects the geometric discontinuity of the channel transition region. When the fillet radius is small, the bracket-root transition is relatively sharp, and the local streamlines are more likely to

undergo sudden deflection. Flow separation and vortices are also more likely to occur near the wall, which promotes high-angle particle impacts. Therefore, the maximum erosion rate is relatively high. When the fillet radius is 2 mm, the maximum erosion rate reaches 1.57×10^{-3} kg·m^{-2}·s^{-1}, indicating that an excessively small fillet radius substantially increases the local erosion risk at the bracket root.

When the fillet radius increases to 3 and 4 mm, the flow transition becomes smoother, and the particle trajectories near the bracket roots become more continuous. As a result, direct particle impact and secondary rebound are weakened. Among the tested cases, the 4 mm fillet gives the lowest maximum erosion rate of 6.06×10^{-4} kg·m^{-2}·s^{-1}, which is lower than those of the 2 and 3 mm schemes. The erosion-rate distributions also show that, as the fillet radius increases, the high-erosion region changes from a concentrated peak to a more dispersed low-intensity erosion zone. This indicates that an appropriate increase in the bracket-root fillet radius can effectively reduce the local erosion peak. Therefore, a 4 mm fillet was selected as the preferred bracket-root transition radius in this study.

3.4.5. Comprehensive Numerical Assessment of the Final Optimized Scheme

Based on the preceding optimization, the final optimized structure was determined as a 45° semi-conical guide hood, two guide brackets, and a 4 mm fillet transition. To evaluate its predicted erosion performance, this combined structure was compared with the baseline structure. The baseline structure used a hemispherical guide hood, three guide brackets, and a 3 mm fillet transition. The simulation boundary conditions, material properties, particle parameters, DPM settings, and Oka erosion-model parameters were identical for the two schemes; only structural parameters were different. The geometries before and after optimization are compared in Figure 18.



(**a**) (**b**)

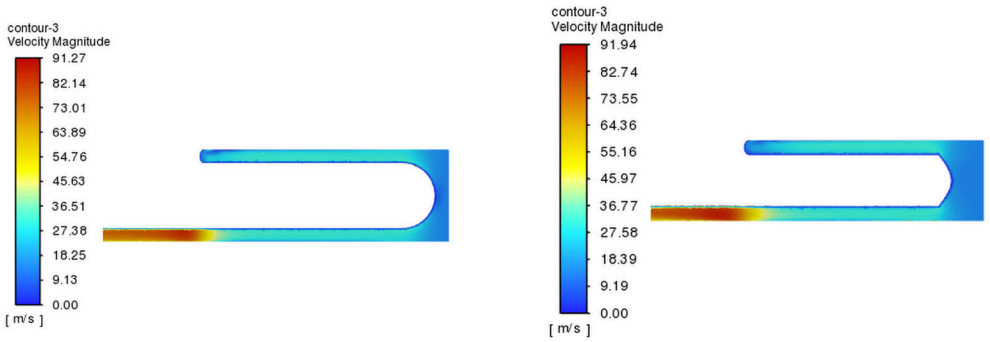
Figure 18. Baseline and optimized structures: (**a**) baseline structure; (**b**) optimized structure.

The velocity distributions of the baseline and optimized structures were compared to evaluate the influence of the optimized structure on the internal flow field, as shown in Figure 19.

Figure 19 suggests a redistribution of local high-speed regions after the guide-hood, support-layout, and fillet changes. Its color-scale maxima are 91.27 m·s^{-1} for the baseline and 91.94 m·s^{-1} for the optimized geometry; thus the optimized result does not show a decrease in the global maximum fluid speed. The lower predicted erosion peak must be assessed through the combined wall-impact loading, particle impact-speed and angle

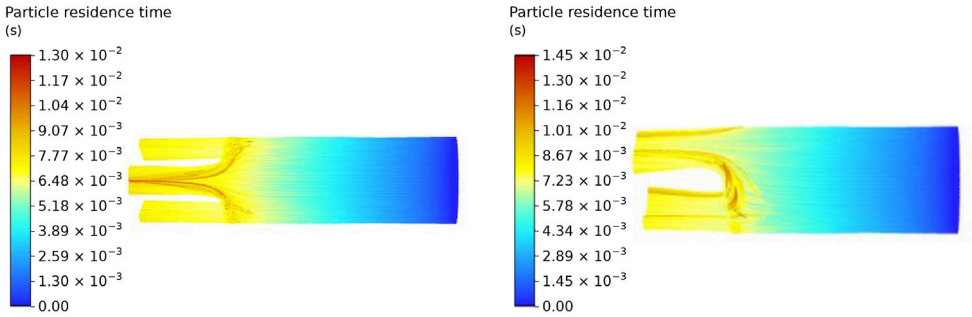
distributions, and hotspot location, rather than inferred from a lower global fluid-speed maximum.

Particle trajectories were further analyzed to determine how the optimized structure affects particle collision behavior, as shown in Figure 20.



(**a**) (**b**)

Figure 19. Comparison of velocity distributions between baseline and optimized structures: (**a**) baseline structure; (**b**) optimized structure.

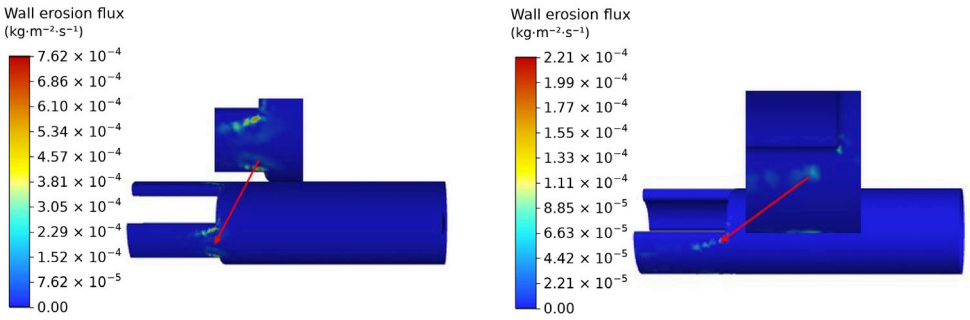


(**a**) (**b**)

Figure 20. Comparison of particle trajectories between baseline and optimized structures: (**a**) baseline structure; (**b**) optimized structure. Colors represent particle residence time in seconds; each panel uses its own scale.

In the baseline structure, particles show obvious deflection near the channel transition and bracket roots. Some particles deviate from the main flow owing to inertia and collide with the wall, forming local erosion concentration. The plotted trajectories for the optimized structure appear smoother near the brackets, suggesting altered particle deflection and secondary collision. Although the maximum particle residence time increases slightly from 1.30×10^{-2} s in the baseline structure to 1.45×10^{-2} s in the optimized structure, no obvious local retention or aggregation zone appears in the particle trajectory; the longer residence time alone does not establish either increased or reduced erosion risk. The reported erosion contour provides the direct numerical comparison of the wall response.

The wall erosion distributions of the baseline and optimized structures are compared in Figure 21, and the comparative numerical results are given in Table 12. We use separate color-scale ranges of 0–7.62×10^{-4} and 0–2.21×10^{-4} kg·m^{-2}·s^{-1} for the baseline and optimized structures, respectively, to resolve local patterns. Identical colors do not indicate equal absolute erosion rates. We interpret hotspot locations and distribution uniformity qualitatively, and assess the reduction in maximum wall-face erosion rate using Table 12. The separate scales do not support comparison of areas above a common absolute erosion threshold.



(**a**) (**b**)

Figure 21. Wall erosion contours of baseline and optimized structures: (**a**) baseline structure; (**b**) optimized structure. Each panel uses a separate color-scale range. Red arrows link enlarged views to the corresponding bracket-root erosion regions.

Table 12. Comparative numerical results for baseline and optimized structures.

Evaluation Indicator	Baseline Structure	Optimized Structure	Change Relative to Baseline
Maximum erosion rate, E_{max} (kg·m^{-2}·s^{-1})	7.62×10^{-4}	2.21×10^{-4}	Approx. 71% lower (model-predicted)
Maximum particle residence time (s)	1.30×10^{-2}	1.45×10^{-2}	Approx. 11.5% higher
Normalized inlet–outlet pressure drop, $\Delta p/\Delta p_{base}$ (dimensionless)	1	0.9815	Approx. 1.85% lower (computed)
Erosion distribution	Localized concentration	More uniform	More uniform (predicted)
High-speed-zone distribution	Concentrated near transition and brackets	Redistributed high-speed regions	Local flow redistribution
Particle trajectory	Obvious deflection and secondary collision at bracket roots	Smoother particle motion	Altered particle deflection

We use the hemispherical guide hood with three guide brackets and a 3 mm bracket-root fillet as the reference for all quantitative changes in Table 12. We calculate relative changes from the optimized-minus-baseline difference divided by the baseline value and express them as percentages; "lower" and "higher" indicate the direction. The tabulated erosion rates and residence times retain three significant figures; the approximately 11.5% residence-time increase follows from the displayed values. We normalize pressure drop by its baseline value, with 0.9815 derived from the reported 1.85% computed reduction.

Optimization reduces the high-erosion regions near the outlet transition and bracket roots and produces a more uniform predicted erosion distribution. At 15 m·s^{-1}, 100 µm and 0.01 kg·s^{-1}, the maximum erosion rate decreases from 7.62×10^{-4} to 2.21×10^{-4} kg·m^{-2}·s^{-1}, an approximately 71% model-predicted reduction. The computed pressure drop decreases by 1.85%, but this difference lacks a pressure-drop-specific uncertainty bound; the E_{max} GCI concerns a different quantity. Both geometries use the same material properties, boundary conditions, models, DPM settings and mesh strategy. The comparison is therefore internally consistent within that framework, while its approximately 71% reduction remains specific to the operating condition and model setup. We use "high-erosion regions" and "more uniform" here as qualitative descriptions of the hotspot patterns, rather than areas above

a shared absolute threshold or a calculated uniformity index. We base the magnitude of the predicted improvement on the tabulated erosion quantities, not on the proportion of a particular color in the separately scaled contours.

The individual optimization studies provide numerical context for the combined result. In the guide-hood series, the 45° semi-conical hood gives an E_{max} value 14.8% below the original hemispherical hood. Within the bracket-number series, the two-wing case is approximately 4.3% below the three-wing case, and within the fillet series, increasing the root fillet from 3 to 4 mm reduces E_{max} by approximately 20.5%. The final baseline-to-optimized comparison gives an approximate 71% reduction. We interpret these one-factor studies as separate controlled comparisons with their respective reference cases. The final 71% value is a direct comparison of the combined configuration. The separate one-factor studies are not a full factorial design and do not quantify interaction terms.

The combined result is consistent with changes in particle diversion by the 45° semi-conical hood, passage subdivision by the two-wing support layout, and transition continuity with the 4 mm fillet. These changes may alter the mass-weighted distribution of impact speed, angle, and repeated wall impacts. In particular, the favorable-angle response of a ductile target is non-monotonic, so reducing impact angle does not necessarily reduce erosion. The contours were used to interpret the combined influence of these geometric changes on erosion distribution.

We selected this combined geometry for its lower predicted erosion peak and small computed pressure-drop decrease under the investigated condition. We also recognize that the brackets provide positioning and support; the erosion calculation alone does not establish the stiffness, load-dependent centering performance or fatigue resistance of the two-wing design. We manufactured the optimized prototype and carried out the functional vibration and simulated-rotation tests described in Section 3.4.6. The sand-laden tests in Section 3.5 assess short-duration erosion under the baseline condition. Static-strength, vibration-fatigue, assembly-reliability and longer-duration erosion tests under a wider range of conditions remain necessary before claiming long-term downhole service reliability.

Tables 13 and 14 summarize the systematic refinement analysis described in Section 2.2, separately from the production-grid comparison in Table 12.

Table 13. Three-dimensional systematic refinement sequences. Values are means of the maximum wall-face erosion flux from five calculations on each mesh, each tracking 2,000,000 particle-parcel trajectories.

Geometry/Grid	Cells N	h (mm)	Mean E_{max} (10^{-4} kg·m^{-2}·s^{-1})
Baseline/coarse 3	526,744	1.164314	7.878
Baseline/medium 2	1,157,257	0.895626	7.752
Baseline/fine 1	2,542,889	0.688907	7.676
Optimized/coarse 3	526,744	1.171182	2.320
Optimized/medium 2	1,157,257	0.900909	2.264
Optimized/fine 1	2,542,889	0.692971	2.230

Table 14. Observed order, fine-grid GCI and Richardson extrapolation.

Geometry	Observed p	Fine-Grid GCI (%)	Extrapolated E_{max} (10^{-4} kg·m^{-2}·s^{-1})
Baseline	1.9275	1.8800	7.560553
Optimized	1.9025	2.9435	2.177488

For both geometries, $r_{21} = 1.30006738$ and $r_{32} = 1.30000016$. We observed a monotonic decrease in the mean maximum wall-face erosion flux for both geometries as we refined the mesh. The baseline and optimized observed orders are 1.9275 and 1.9025, with fine-grid GCIs of 1.88% and 2.94%, respectively. The asymptotic ratios $GCI_{32}/(r_{21}{}^{p}GCI_{21})$ are 0.9902 and 0.9850, respectively, close to unity. During refinement, we recorded peak-position shifts of 0.20 mm for the baseline structure and 0.32 mm for the optimized structure in their respective root-surface coordinate systems. We use these shifts to describe the computed peak locations within the refinement sequences; they do not quantify peak-position uncertainty on the separate production mesh. The fine-grid comparison gives $1 - 2.230/7.676 = 70.95\%$ reduction, supporting the trend of the production-grid comparison, $1 - 2.21/7.62 \approx 71\%$. From the corresponding coarse-, medium- and fine-grid values in Table 13, we obtain predicted reductions of 70.55%, 70.79% and 70.95%, respectively. Their consistency with the approximately 71% production-grid comparison supports the stability of the baseline-to-final structural trend but does not assign a GCI bound to the production-grid peaks. We interpret the observed orders and GCIs conditionally because the grid-level means alone do not quantify residual tracking variability. The near-unity asymptotic ratios check consistency within these refinement sequences and do not replace a separate assessment of particle-sampling variation.

Applying the two fine-grid GCI estimates in opposite directions gives a discretization-only reduction envelope of 69.52–72.32%. Its lower limit is $1 - [2.230(1 + 0.029435)]/[7.676(1 - 0.018800)]$, and its upper limit reverses the two signs. This constructed envelope is neither a confidence interval nor a total-uncertainty interval. It applies to these refinement sequences and cannot be transferred to the production-grid peaks or used to assess the 1.85% pressure-drop difference.

3.4.6. Prototype-Level Functional Verification of the Optimized Tool

We manufactured a prototype of the optimized tool and evaluated its measurement functionality on our laboratory platform under the specified test conditions. The internal system comprised a single-axis IEPE piezoelectric accelerometer (353B01; ±250 g measurement range and 20 mV/g sensitivity), a Class A M222 Pt100 thin-film platinum resistance temperature sensor (YAGEO Nexensos GmbH, Kleinostheim, Germany; Class A accuracy specified over −50 to 300 °C), the existing laboratory signal-processing and storage board, and a host-computer acquisition program developed in-house. One accelerometer was mounted horizontally, and signals were sampled at 10 kHz. The manufacturer specifies a shock overload limit of ±10,000 g for the accelerometer; this component rating does not represent experimentally verified shock resistance of the assembled tool. We installed the prototype at the drill-bit central-waterway position used in the structural design. Simulated-rotation tests used an existing non-standard laboratory-integrated downhole-tool dynamic simulation platform at 10–50 r/min. The assembled prototype and the simulated drill-bit rotation platform are shown in Figure 22. Grid-convergence and erosion results are reported separately in Sections 3.4.5 and 3.5.

We carried out three groups of tests. In the static test, the raw acceleration baseline fluctuated around 0.25 g and the temperature variation remained within 1 °C over 30 min. In the controlled-impact test, we released a 500 g steel ball from heights of 0.2, 0.5, and 1.0 m and repeated each condition three times. The measured acceleration extrema were +5.19/−4.98 g, +12.53/−20.25 g, and +35.73/−32.7 g, respectively. The increasing response magnitude with drop height demonstrates that the prototype resolves different levels of transient mechanical excitation over the tested range.

In simulated-rotation tests at 10–50 r/min, the representative nominal 10 r/min case tracked the startup trend. During steady operation, the tool measured a mean of

10.18 r/min against 9.46 r/min from the platform, a 7.6% relative deviation using the platform mean as denominator; the maximum instantaneous difference was approximately 1 r/min (Figure 23). Similar response patterns were observed at the other tested speeds. These tests demonstrate assembly feasibility and basic vibration/rotation measurement function under laboratory conditions. They do not quantify support stiffness, load-induced eccentricity, root stress or fatigue life, and do not reproduce sand-laden erosion. Section 3.5 reports the separate erosion measurements.



Figure 22. Prototype-level laboratory verification setup: (**a**) optimized tool installed in the drill-bit central waterway; (**b**) experimental platform for simulated drill-bit rotation. The Chinese lettering on the rig identifies the laboratory downhole-tool simulation test platform; the display retains the platform's original control-interface labels.

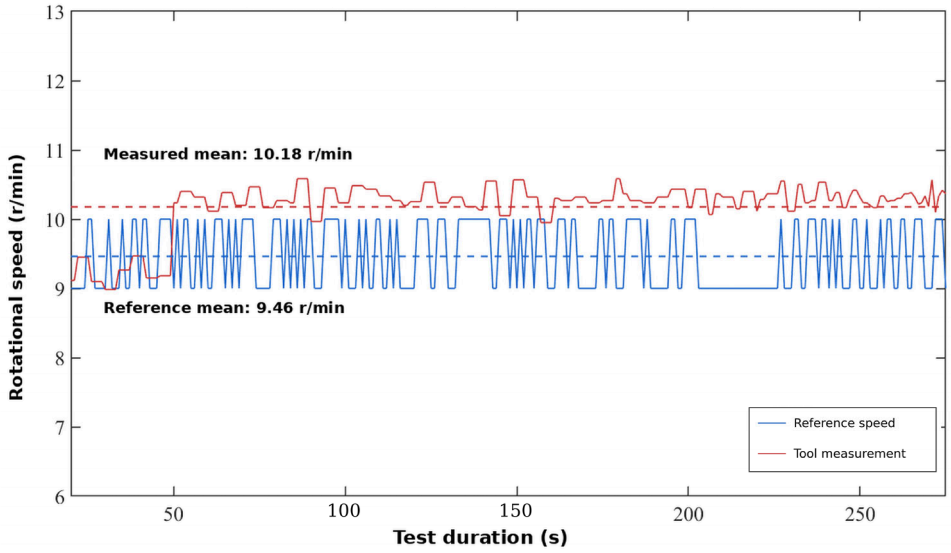


Figure 23. Comparison between the tool-measured rotational speed and the reference rotational speed in a representative nominal 10 r/min test, including startup and steady operation. Blue and red solid curves denote the reference speed and tool measurement, respectively; dashed lines indicate their reported means.

3.5. Sand-Laden Erosion Test Results

The tests followed the conditions and measurement definitions in Section 2.7. Table 15 lists the six independent specimen results after the common 0.002 g blank correction. Baseline local wear was concentrated at the upstream bracket-root transition, whereas optimized local wear occurred at the downstream fillet transition.

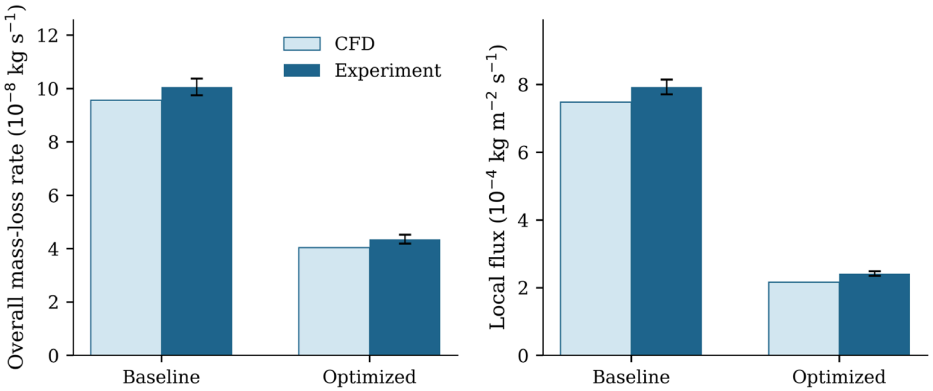
Table 15. Blank-corrected mass loss and registered local-window depth after 1800.0 s (B: baseline; O: optimized).

Specimen	Net Loss (g)	Window Depth Δh (µm)
B1	0.180	181.0
B2	0.187	187.0
B3	0.176	177.0
O1	0.079	54.0
O2	0.075	57.0
O3	0.081	55.0

Baseline and optimized net mass losses were 0.1810 ± 0.0056 g and 0.0783 ± 0.0031 g (mean ± sample SD, $n = 3$). Overall mass-loss rates were 1.006×10^{-7} and 4.352×10^{-8} kg·s^{-1}, a 56.72% reduction. Local-window depths were 181.7 ± 5.0 and 55.3 ± 1.5 µm, giving depth rates of 1.009×10^{-7} and 3.074×10^{-8} m·s^{-1}, a 69.54% reduction. Derived percentages use the unrounded specimen means. These spatial measures differ from the approximately 71% CFD maximum-face reduction.

Using the reported mean fluxes and wall areas gives CFD wall integrals of $(8.10 \times 10^{-7})(0.1180) = 9.558 \times 10^{-8}$ kg·s^{-1} and $(3.61 \times 10^{-7})(0.1120) = 4.043 \times 10^{-8}$ kg·s^{-1}. The experimental overall rates exceed the respective CFD estimates by 5.21% and 7.63%; the window fluxes exceed their matched CFD values by 5.92% and 11.72%. Each deviation uses the CFD value as the denominator and is calculated from unrounded inputs. CFD wall-integral and matched-window reductions are approximately 57.70% and 71.12%, compared with measured reductions of 56.72% and 69.54%. These comparisons concern matched spatial measures and do not measure the maximum wall-face flux.

Figure 24 compares overall mass-loss rates in panel (a) and registered local-window fluxes in panel (b). Experimental error bars show mean ± sample SD for three independent specimens per geometry; CFD columns are point estimates without total-uncertainty intervals. These separate spatial comparisons do not validate a single-face erosion peak.



(a) Overall mass loss (b) Registered local window

Figure 24. Spatially matched CFD and sand-laden test comparisons: (**a**) overall mass-loss rate; (**b**) registered 0.20 × 0.20 mm local-window flux. Experimental bars show mean ± sample SD (three independent specimens per geometry); CFD columns are point estimates without total-uncertainty intervals. Test conditions: 15 m·s^{-1}, 100 µm, 0.01 kg·s^{-1} and 1800 s.

Independent-specimen repeatability alone gives first-order standard uncertainties of 0.012411 and 0.006878 for the optimized-to-baseline overall-loss and local-depth ratios, equivalent to 1.241 and 0.688 percentage points in the reductions ($k = 1$). Full ratio uncertainties also require common-blank covariance and the other components in Section 2.7. The

point-estimate deviations in Table 16 are descriptive differences, not validation acceptance criteria. The tests support short-duration mitigation; they do not establish absolute peak accuracy or long-term downhole performance.

Table 16. Spatially matched comparisons of CFD and experimental means.

Matched Quantity	Baseline	Optimized
Measured overall loss rate ($kg \cdot s^{-1}$)	1.006×10^{-7}	4.352×10^{-8}
CFD wall integral ($kg \cdot s^{-1}$)	9.558×10^{-8}	4.043×10^{-8}
Measured window flux ($kg \cdot m^{-2} \cdot s^{-1}$)	7.923×10^{-4}	2.413×10^{-4}
CFD matched-window flux ($kg \cdot m^{-2} \cdot s^{-1}$)	7.48×10^{-4}	2.16×10^{-4}

4. Discussion

Predicted erosion is localized at channel transitions and bracket roots. The correspondence between computed flow changes, particle deflection and wall-flux hotspots is consistent with geometry-dependent impact loading. It provides a physical interpretation of the structural comparisons, but does not separately quantify speed, angle and repeated-impact contributions.

The comparisons also show that streamline smoothness alone is an insufficient design criterion. In the adopted ductile-target model, impact-angle response is non-monotonic; selection must consider the combined mass-weighted erosion flux. Unresolved smaller differences, including the 4.3% two-/three-bracket comparison and the 1.85% pressure-drop change, require quantity- and geometry-specific uncertainty assessment.

The evidence has three distinct scopes. The separate fine-grid sequences support the predicted structural trend. Prototype tests establish sensing function under laboratory conditions. Sand-laden tests compare short-duration overall mass loss and local-window wear in simplified, full-scale core assemblies. Their reductions of 56.72% and 69.54% apply to the specified 1800 s baseline-condition tests, with three independent specimens per geometry.

The approximately 71% reduction refers specifically to the maximum wall-face erosion flux predicted by CFD–DPM. This quantity differs from both the whole-assembly mass-loss rate and the spatially averaged local-window measurement. The comparisons in Section 3.5 use the CFD wall integral for overall mass loss and the matched-window flux for local wear. This evidence applies to the nominal baseline condition and assumes consistent inlet-section and exposed-wall definitions. Although these spatially matched comparisons provide experimental support for the predicted erosion mitigation, they do not directly validate the maximum-face-flux reduction. The approximately 71% value therefore remains a condition-specific numerical prediction requiring further experimental confirmation using a consistently defined local erosion metric and an appropriate uncertainty assessment. The present results do not establish long-term downhole durability or a universal reduction factor. The 1.85% computed pressure-drop decrease lacks its own uncertainty assessment.

We assessed grid sensitivity using evaluation quantities matched to each purpose. Our five-mesh assessment of pressure drop and area-averaged erosion guided the production-mesh selection. For the baseline and final optimized geometries, our separate refinement sequences examined the mean maximum wall-face erosion flux over a wall set that includes the bracket-root and fillet regions. We obtained fine-grid GCIs of 1.88% and 2.94% and a fine-grid erosion reduction of 70.95%, supporting the stability of the predicted structural trend within these sequences. We do not transfer these indices to the separate production-grid peaks or to every intermediate geometry and operating condition. The indices exclude

particle-sampling variation and erosion-model uncertainty, so we interpret smaller differences among other design alternatives cautiously.

The guide brackets transmit loads between the tool body and mounting sleeve while partitioning the annular flow passage. We retained the total supporting cross-sectional area in the bracket-number comparison, but changing from three to two brackets redistributes the circumferential load paths. This redistribution may affect directional stiffness and the vibration response of the assembly. Under lateral loading, support deformation could produce eccentric displacement and change the local annular clearance; the coaxial design and successful assembly do not quantify this load-dependent centering behavior. Repeated vibration and impact also require an assessment of cyclic stresses at the bracket roots and transition regions. Our erosion calculations and functional tests do not quantify these mechanical responses. We therefore regard the two-wing arrangement as the preferred configuration for erosion mitigation within the investigated cases, with its structural strength, centering performance and fatigue resistance requiring separate evaluation.

The simulations use spherical particles and steady flow at the specified fluid properties and operating conditions. Particle morphology, size distribution, fragmentation, bit rotation, tool vibration, and high-temperature and high-pressure downhole conditions remain outside this model's scope.

Irregular particle shape and orientation can alter drag and particle response to the flow, changing slip velocity and wall-impact locations [32]. Grain angularity and contact orientation can also change rebound speed and direction and the distribution of secondary impacts [33]. Particle shape may further affect cutting and plowing during material removal [17,18]. The erosion parameters may reflect original calibration-particle characteristics, but our model does not explicitly resolve individual irregular-grain geometry and orientation. We have not quantified the tool's sensitivity to sand morphology, so we cannot assign a systematic direction or magnitude to the resulting erosion bias. We interpret the predicted peaks and reductions within the spherical-particle representation; shared assumptions do not demonstrate cancellation of shape effects between geometries. Neither the DPM repeat ranges nor the GCIs quantify this model limitation.

We interpret the regression statistics as fit quality, without establishing independent predictive accuracy. Our overall mass-loss and local-wear measurements do not validate the regression for maximum wall-face flux across its input range. We require separate validation for untested combinations, geometries and operating conditions, and use direct CFD-DPM comparisons for structural selection.

Our 1800 s tests provide a short-duration benchmark for further validation. We propose three stages. First, one-factor tests of both geometries would vary inlet velocity, particle size or sand feed while retaining the other baseline inputs. Candidate conditions are 10, 15 and 20 $m \cdot s^{-1}$; 100, 200 and 400 μm; and 0.005, 0.010 and 0.020 $kg \cdot s^{-1}$, subject to test-rig capacity. We would use independent specimens and consistent inlet-section, exposed-wall, blank-correction and window-registration definitions to compare pressure drop, overall mass loss, local depth and geometry with spatially matched CFD quantities. These local comparisons would use matched spatial averaging scales, account for hotspot migration, and include measurement-uncertainty assessment. Second, candidate exposures of 1800, 3600 and 7200 s would assess wear progression, hotspot migration and morphology. Successive exposures of the same specimen would be treated as repeated measurements. Third, we would compare the baseline and optimized assemblies under consistent mounting constraints and representative axial, lateral and torsional loads, quantifying bracket-root stress and load-dependent displacement. Modal and cyclic-loading assessments would address vibration response and fatigue resistance. We would also examine assembly condition and sensing function under rotation and vibration before tests closer to downhole conditions. Further

numerical work would examine geometry-detail sensitivity and pressure-drop-specific uncertainty alongside the peak-flux grid assessment. We would also characterize sand-grain morphology and assess shape-dependent drag and rebound under matched particle-size, material and flow conditions.

5. Conclusions

A CFD-DPM framework combining the realizable k-ε turbulence, Forder rebound and Oka erosion models was used to analyze and optimize a drill-bit-integrated vibration detection tool. We interpret the numerical parameter trends and structural comparisons within the adopted spherical-particle representation. Prototype tests assessed sensing function, while sand-laden tests measured overall mass loss and local wear. The main conclusions are as follows.

1. The coaxial tool arrangement inside the central waterway of a 241 mm PDC drill bit accommodates sealed sensing components while maintaining an external annular fluid passage. The guide hood, mounting sleeve and brackets provide flow diversion, positioning and support; their transitions are therefore central to erosion-resistant design.
2. Baseline erosion is concentrated at the channel transition and guide-bracket roots, with a predicted maximum erosion rate of 7.62×10^{-4} kg·m^{-2}·s^{-1}. Local acceleration, particle deflection and wall-impact loading identify these transitions as the principal targets for structural optimization.
3. Across the investigated ranges, inlet velocity produces the largest predicted response: E_{max} rises from 5.70×10^{-5} to 2.92×10^{-3} kg·m^{-2}·s^{-1} between 5 and 25 m·s^{-1}. Particle mass flow rate produces an approximately linear increase. The particle-size response is non-monotonic, with 200 μm the most erosive of the four tested sizes. The exact peak diameter remains unresolved, and the overlapping 300 and 400 μm ranges do not support a stable ranking.
4. We obtained an empirical description of the fitted baseline-geometry simulation data in terms of inlet velocity, particle diameter and particle mass flow rate, with $R^2 = 0.8301$ and adjusted $R^2 = 0.8281$. We restrict this relation to the represented conditions and numerical assumptions; untested combinations and other geometries require further validation. Structural selection was based on the case-by-case simulation results and erosion distributions.
5. Within the investigated cases, we selected a 45° semi-conical guide hood, two guide brackets and a 4 mm bracket-root fillet as the preferred combination for erosion mitigation. Their joint changes to particle diversion, passage subdivision and transition continuity redistribute the predicted erosion; the separate one-factor improvements are not additive contributions to the final reduction.
6. Under the baseline numerical condition, optimization reduces E_{max} from 7.62×10^{-4} to 2.21×10^{-4} kg·m^{-2}·s^{-1}, approximately 71%. In the separate refinement sequences, we obtained a fine-grid reduction of 70.95% and fine-grid GCIs of 1.88% and 2.94% for the baseline and final optimized geometries, respectively. These results support the case-specific peak-reduction trend. We use these indices to characterize the corresponding fine-grid solutions; they do not provide uncertainty bounds for the production-grid peaks. The approximately 71% reduction remains a numerical prediction and has not been directly validated experimentally. The computed 1.85% pressure-drop decrease has no pressure-drop-specific uncertainty assessment.
7. The optimized prototype maintained stable signal acquisition in static, controlled-impact, and simulated-rotation laboratory tests. The measured impact-response amplitude increased consistently with impact severity, and the representative steady-rotation test showed a 7.6% relative deviation between the tool measurement and the reference

platform. These tests support the functional feasibility of the optimized structure but do not constitute direct validation of the CFD erosion rate. We do not infer the stiffness, load-dependent centering accuracy or fatigue resistance of the two-wing support from these functional results.

8. At 15 $m \cdot s^{-1}$, 100 μm and 0.01 $kg \cdot s^{-1}$, three independent specimens per geometry exposed for 1800 s showed reductions of 56.72% in overall mass-loss rate and 69.54% in local-window depth rate. Comparisons used the CFD wall integral and a matched 0.20 × 0.20 mm window, respectively. The results support short-duration erosion mitigation without establishing a 71% experimental peak reduction or long-term downhole durability.

Author Contributions: Conceptualization, J.J.; methodology, J.J. and Z.J.; validation, C.Y. and Y.X.; formal analysis, J.J.; investigation, Y.X.; resources, C.Y.; data curation, Z.J.; writing—original draft preparation, J.J.; writing—review and editing, L.S. and Y.X.; visualization, Z.J.; supervision, L.S.; project administration, L.S.; funding acquisition, L.S. All authors have read and agreed to the published version of the manuscript.

Funding: This research was funded by the National Natural Science Foundation of China, grant number 52204002.

Institutional Review Board Statement: Not applicable.

Informed Consent Statement: Not applicable.

Data Availability Statement: Detailed industrial project files, including original numerical models and some engineering test records, are subject to confidentiality and data-control requirements of the industrial partner and cannot be publicly disclosed. The reported comparisons, DPM repeat records and observed minimum–maximum endpoints, GCI summaries, and individual sand-test mass-loss and local-depth results are provided in the tables and figures; access to additional records requires permission from the industrial partner.

Conflicts of Interest: Author Chen Yu is affiliated with CNPC Bohai Drilling Engineering Co., Ltd. The remaining authors declare no conflicts of interest.

References

1. Ghasemloonia, A.; Rideout, D.G.; Butt, S.D. A review of drillstring vibration modeling and suppression methods. *J. Pet. Sci. Eng.* **2015**, *131*, 150–164. [CrossRef]
2. Nandakumar, K.; Wiercigroch, M. Stability analysis of a state dependent delayed, coupled two DOF model of drill-string vibration. *J. Sound Vib.* **2013**, *332*, 2575–2592. [CrossRef]
3. Kapitaniak, M.; Vaziri Hamaneh, V.; Páez Chávez, J.; Nandakumar, K.; Wiercigroch, M. Unveiling complexity of drill-string vibrations: Experiments and modelling. *Int. J. Mech. Sci.* **2015**, *101–102*, 324–337. [CrossRef]
4. Chen, S.; Wisinger, J.; Dunbar, B.; Propes, C. Identification and mitigation of friction- and cutting-action-induced stick/slip vibrations with PDC bits. *SPE Drill. Complet.* **2020**, *35*, 576–587. [CrossRef]
5. Di, Q.F.; Ping, J.C.; Li, N.; Wang, W.; Wang, M.; Zhang, H. Progress in measurement technology for drill string vibration. *Mech. Eng.* **2015**, *37*, 565–579. (In Chinese) [CrossRef]
6. Macpherson, J.D.; Jogi, P.N.; Kingman, J.E.E. Application and analysis of simultaneous near-bit and surface dynamics measurements. *SPE Drill. Complet.* **2001**, *16*, 230–238. [CrossRef]
7. Liu, W.; Zhou, Y.C.; Wang, Y.; Zhai, X. Study on downhole vibration measurement and analysis principles. *Oil Drill. Prod. Technol.* **2012**, *34*, 14–18. (In Chinese) [CrossRef]
8. Zhai, X.Q.; Wang, Y.; Liu, W.; Ji, R. Design and laboratory test of a memory-type downhole vibration measurement tool. *Pet. Drill. Tech.* **2011**, *39*, 111–114. (In Chinese) [CrossRef]
9. Parsi, M.; Najmi, K.; Najafifard, F.; Hassani, S.; McLaury, B.S.; Shirazi, S.A. A comprehensive review of solid particle erosion modeling for oil and gas wells and pipelines applications. *J. Nat. Gas Sci. Eng.* **2014**, *21*, 850–873. [CrossRef]
10. Forder, A.; Thew, M.; Harrison, D. A numerical investigation of solid particle erosion experienced within oilfield control valves. *Wear* **1998**, *216*, 184–193. [CrossRef]

11. Mansouri, A.; Arabnejad, H.; Shirazi, S.A.; McLaury, B.S. A combined CFD/experimental methodology for erosion prediction. *Wear* **2015**, *332–333*, 1090–1097. [CrossRef]
12. Finnie, I. Erosion of surfaces by solid particles. *Wear* **1960**, *3*, 87–103. [CrossRef]
13. Bitter, J.G.A. A study of erosion phenomena, part I. *Wear* **1963**, *6*, 5–21. [CrossRef]
14. Bitter, J.G.A. A study of erosion phenomena, part II. *Wear* **1963**, *6*, 169–190. [CrossRef]
15. Grant, G.; Tabakoff, W. Erosion prediction in turbomachinery resulting from environmental solid particles. *J. Aircr.* **1975**, *12*, 471–478. [CrossRef]
16. Levy, A.V. The erosion of structural alloys, cermets and in situ oxide scales on steels. *Wear* **1988**, *127*, 31–52. [CrossRef]
17. Oka, Y.I.; Okamura, K.; Yoshida, T. Practical estimation of erosion damage caused by solid particle impact: Part 1: Effects of impact parameters on a predictive equation. *Wear* **2005**, *259*, 95–101. [CrossRef]
18. Oka, Y.I.; Yoshida, T. Practical estimation of erosion damage caused by solid particle impact: Part 2: Mechanical properties of materials directly associated with erosion damage. *Wear* **2005**, *259*, 102–109. [CrossRef]
19. Shih, T.H.; Liou, W.W.; Shabbir, A.; Yang, Z.; Zhu, J. A new k-ε eddy viscosity model for high Reynolds number turbulent flows. *Comput. Fluids* **1995**, *24*, 227–238. [CrossRef]
20. Arabnejad, H.; Mansouri, A.; Shirazi, S.A.; McLaury, B.S. Development of mechanistic erosion equation for solid particles. *Wear* **2015**, *332–333*, 1044–1050. [CrossRef]
21. Vieira, R.E.; Mansouri, A.; McLaury, B.S.; Shirazi, S.A. Experimental and computational study of erosion in elbows due to sand particles in air flow. *Powder Technol.* **2016**, *288*, 339–353. [CrossRef]
22. Duarte, C.A.R.; Souza, F.J.; Santos, V.F. Mitigating elbow erosion with a vortex chamber. *Powder Technol.* **2016**, *288*, 6–25. [CrossRef]
23. Wang, J.; Shirazi, S.A. A CFD based correlation for erosion factor for long-radius elbows and bends. *J. Energy Resour. Technol.* **2003**, *125*, 26–34. [CrossRef]
24. McLaury, B.S.; Shirazi, S.A. An alternate method to API RP 14E for predicting solids erosion in multiphase flow. *J. Energy Resour. Technol.* **2000**, *122*, 115–122. [CrossRef]
25. Zhang, Z.; An, C.; Wei, D.F.; Wang, Z.G. Sand erosion study of subsea choke valve based on numerical simulation. *Ocean Eng.* **2022**, *40*, 160–172. (In Chinese) [CrossRef]
26. Wang, Z.Y.; Yang, H.M.; Zhang, Y.Y.; Liu, X. Research progress on erosion theory and prediction in pipe string of gas storage. *Surf. Technol.* **2023**, *52*, 91–110. (In Chinese) [CrossRef]
27. Yao, M.J.; Li, C.F.; He, J.B.; Hou, Y. Progresses of anti-erosion coatings. *Mater. Rev.* **2015**, *29*, 283–286. (In Chinese)
28. Xie, Z.; Cao, X.; Li, Q.; Yao, H.; Qin, R.; Sun, X. Experimental study on particle movement and erosion behavior of the elbow in liquid–solid flow. *Heliyon* **2023**, *9*, e21275. [CrossRef]
29. Celik, I.B.; Ghia, U.; Roache, P.J.; Freitas, C.J.; Coleman, H.; Raad, P.E. Procedure for estimation and reporting of uncertainty due to discretization in CFD applications. *J. Fluids Eng.* **2008**, *130*, 078001. [CrossRef]
30. Morsi, S.A.; Alexander, A.J. An investigation of particle trajectories in two-phase flow systems. *J. Fluid Mech.* **1972**, *55*, 193–208. [CrossRef]
31. Joint Committee for Guides in Metrology. *Evaluation of Measurement Data—Guide to the Expression of Uncertainty in Measurement*; JCGM 100:2008; BIPM: Sèvres, France, 2008. Available online: https://www.bipm.org/documents/20126/2071204/JCGM_100_2008_E.pdf (accessed on 25 October 2026).
32. Hölzer, A.; Sommerfeld, M. New simple correlation formula for the drag coefficient of non-spherical particles. *Powder Technol.* **2008**, *184*, 361–365. [CrossRef]
33. Sommerfeld, M.; Huber, N. Experimental analysis and modelling of particle-wall collisions. *Int. J. Multiph. Flow* **1999**, *25*, 1457–1489. [CrossRef]

Disclaimer/Publisher's Note: The statements, opinions and data contained in all publications are solely those of the individual author(s) and contributor(s) and not of MDPI and/or the editor(s). MDPI and/or the editor(s) disclaim responsibility for any injury to people or property resulting from any ideas, methods, instructions or products referred to in the content.